GEOFLUIDS

Geofluids (2014) **14**, 20–44 doi: 10.1111/gfl.12021

Polyphasic hydrothermal and meteoric fluid regimes during the growth of a segmented fault involving crystalline and carbonate rocks (Barcelona Plain, NE Spain)

I. CANTARERO, A. TRAVÉ, G. ALÍAS AND V. BAQUÉS

Departament de Geoquímica, Petrologia i Prospecció Geologica, Facultat de Geologia, Universitat de Barcelona (UB), Barcelona, Spain

ABSTRACT

A polyphasic tectonic-fluid system of a fault that involves crystalline and carbonate rocks (Hospital fault, Barcelona Plain) has been inferred from regional to thin section scale observations combined with geochemical analyses. Cathodoluminescence, microprobe analyses and stable isotopy in fracture-related cements record the circulation of successive alternations of hydrothermal and low-temperature meteoric fluids linked with three main regional tectonic events. The first event corresponds to the Mesozoic extension, which had two rifting stages, and it is characterized by the independent tectonic activity of two fault segments, namely southern and northern Hospital fault segments. During the Late Permian-Middle Jurassic rifting, these segments controlled the thickness and distribution of the Triassic sediments. Also, dolomitization was produced in an early stage by Triassic seawater at shallow conditions. During increasing burial, formation of fractures and their dolomite-related cements took place. Fault activity during the Middle Jurassic–Late Cretaceous rifting was localized in the southern segment, and it was characterized by hydrothermal brines, with temperatures over 180°C, which ascended through this fault segment precipitating quartz, chlorite, and calcite. The second event corresponds to the Paleogene compression (Chattian), which produced exhumation, folding and erosion, favouring the percolation of low-temperature meteoric fluids which produced the calcitization of the dolostones and of the dolomite cements. The third event is linked with the Neogene extension, where three stages have been identified. During the syn-rift stage, the southern segment of the Hospital fault grew by tip propagation. In the relay zone, hydrothermal brines with temperature around 140°C upflowed. During the late postrift, the Hospital fault acted as a unique segment and deformation occurred at shallow conditions and under a low-temperature meteoric regime. Finally, and possibly during the Messinian compression, NW-SE strike-slip faults offset the Hospital fault to its current configuration.

Key words: Barcelona Plain, crystalline basement, fracture-related cements, hydrothermal fluids, segmented fault

Received 27 July 2012; accepted 1 February 2013

Corresponding author: Irene Cantarero, Departament de Geoquímica, Petrologia i Prospecció Geològica, Facultat de Geologia, Universitat de Barcelona (UB), Martí i Franquès s/n, Barcelona 08028, Spain.
E-mail: i_cantarero@ub.edu. Tel.: +34 934031165. Fax: +34 934021340.

Geofluids (2014) **14**, 20–44

INTRODUCTION

Fault zones play an important control in fluid flow because of their behavior as conduits or barriers to fluids (Caine *et al.* 1996; Rowland & Sibson 2004). The behavior of the fault zone is controlled by its architecture (Berg & Skar 2005) and the petrophysical properties of the fault rocks (porosity, permeability, cohesivity, etc.), which vary spatially and temporally along the fault. The petrophysical properties can change due to grain comminution and mineral neoformation, processes that are in turn controlled by the lithology, pressure-temperature conditions, and physico-chemical characteristics of fluids. Minerals formed during circulation of fluids coeval to fracturing record important information about the evolution of the fault zone architecture, the deformation mechanisms, and the types of fluids during fault history (O'Kane *et al.* 2007; Breesch *et al.* 2009; Travé *et al.* 2009). The reactivation of faults can produce changes in fault behavior and the mobilization of fluids, consequently controlling fluid flow and

preservation of structural traps, point of high interest due to their relation with economic geology and petroleum geology (Zhang *et al.* 2009). In addition, most of the works that study the fault-fluid evolution within the brittle regime, which are focused on one lithology, normally in carbonate rocks (Labaume *et al.* 2004; Micarelli *et al.* 2006; Bussolotto *et al.* 2007; Bastesen *et al.* 2009; Breesch *et al.* 2009; Andre *et al.* 2010; Baqués *et al.* 2010, 2012; Billi 2010; Rodríguez-Morillas *et al.* 2013) or siliciclastic rocks (Labaume & Moretti 2001; Travé & Calvet 2001; Boles *et al.* 2005; Davatzes & Aydin 2005; Eichhubl *et al.* 2009; Onasch *et al.* 2009; Travé *et al.* 2009), as these rocks constitute most of reservoirs. However, due to the high demand of energetic resources, unconventional reservoirs, such as crystalline basement reservoirs, have increased their interest and more studies about deformation and fluids in crystalline rocks need to be done. Therefore, a multidisciplinary study based on multiscale structural analysis and petrological and geochemical data of fracture-related cements leads to decipher the origin and the pathways of fluids.

The present study has been focused on unravel the successive fault–fluid systems on a segmented fault that grew and was reactivated by two extensional and one compressional event. This fault is located at the Barcelona Plain (Catalan Coastal Ranges) and juxtaposes Triassic carbonates and Miocence siliciclastic rocks against basement granodiorites. The presence of different lithologies forming the footwall and hanging-wall of the fault zone allows us to study the host rock influence on the mineralogical changes and precipitation of neoformed minerals within the fault zone and the effects of the fluids circulating through the faults, that is, it allows us to study the fault–fluid–rock interaction through time from the cover to the basement. The aims of this study are fourfold: (i) to characterize petrologically and geochemically the successive generations of fault rocks and cements along a segmented fault and its hanging-wall; (ii) to determine the composition and origin of the fluids that circulated through the faults; (iii) to establish the hydrogeological regimes and the fluid pathways as a function of the involved tectonic event; and (iv) to determine the factors that control fault zone heterogeneities.

GEOLOGICAL SETTING

The Barcelona Plain and its boundary faults locate within the Catalan Coastal Ranges (CCR). These ranges form the western margin of the Valencia Trough (Fig. 1), an extensional basin located between the Iberian Peninsula and the Balearic Promontory. The CCR are the result of the superposition of three main tectonic events. During the Mesozoic, two rift stages related with the opening of the western Tethys and of the North Atlantic took place (Salas & Casas 1993; Rossi *et al.* 2001). The first rift stage lasted from Late Permian to Middle Jurassic and the second one occurred during the Late Jurassic–Late Cretaceous times. The normal faults generated during this period were later reactivated as thrust faults during the N-S compression caused by the collision of the Iberian and European plates (Late Cretaceous-early Oligocene) (Bartrina *et al.* 1992). This positive inversion had a limited left-lateral motion (Ashauer & Teichmüller 1935; Anadón *et al.* 1985; Roca 1996). In the studied area, the compressive structures correspond to the very late compressive stage (Chattian) (Parcerisa 2002). During the Neogene extension (late Oligocene-middle Miocene), faults were again reactivated as normal faults. This late extensional process, responsible of the opening of the Valencia Trough, is related to the southwestward propagation of the Western European rift system and the Burdigalian oceanic accretion associated with the counterclockwise rotation of the Corsica-Sardinia block from the European margin to its current position (Cherchi & Montadert 1982; Roca *et al.* 1999). This last event of deformation was the responsible of the actual morphology of the CCR, which is characterized by a system of horsts and grabens limited by listric faults striking NE-SW and NNE-SSW with a detachment level at 12–16 km (Fig. 1) (Gaspar-Escribano *et al.* 2004). This structure is also offset by later faults trending NW-SE to NNW-SSE. The tectonic evolution of the CCR during the Neogene extension is divided into a syn-rift stage (late Oligocene-late Burdigalian), an early postrift stage (late Burdigalian-early Serravalian) and a late postrift stage (Serravalian to Present). Within the postrift, two small compressional stages have been recognized: one during the early postrift (Langhian-Serravalian) and one during the late postrift (Messinian) (Calvet *et al.* 1996; Gaspar-Escribano *et al.* 2004).

Abundant springs, some of them of hot water (up to 70°C), occur in the intersection between the main faults limiting the grabens and the last NW-SE faults (Fernández & Banda 1989). These hot springs, which are exploited as spa since the roman times, are preferably located in the igneous basement, which constitutes the footwall of the faults, that is, Caldes de Montbui, La Garriga, Caldes d'Estrac (Fig. 1) (Albert *et al.* 1979; Carmona *et al.* 2000). Fault-controlled barite–fluorite–sulphur veins along the CCR (Canals & Cardellach 1997; Piqué *et al.* 2008) have been interpreted as the result of two hydrothermal events: a Mesozoic (at least Jurassic) and a Neogene (lower Miocene) event (Cardellach *et al.* 2002).

The studied area is located within the Barcelona Plain, a graben about 40 km long and 2–10 km wide situated in the central sector of the CCR (Figs 1 and 2). Its filling mainly consists of Miocene continental-transitional siliciclastic deposits and Quaternary fluvio-deltaic deposits. Its northern boundary is limited by the Collserola-Montnegre

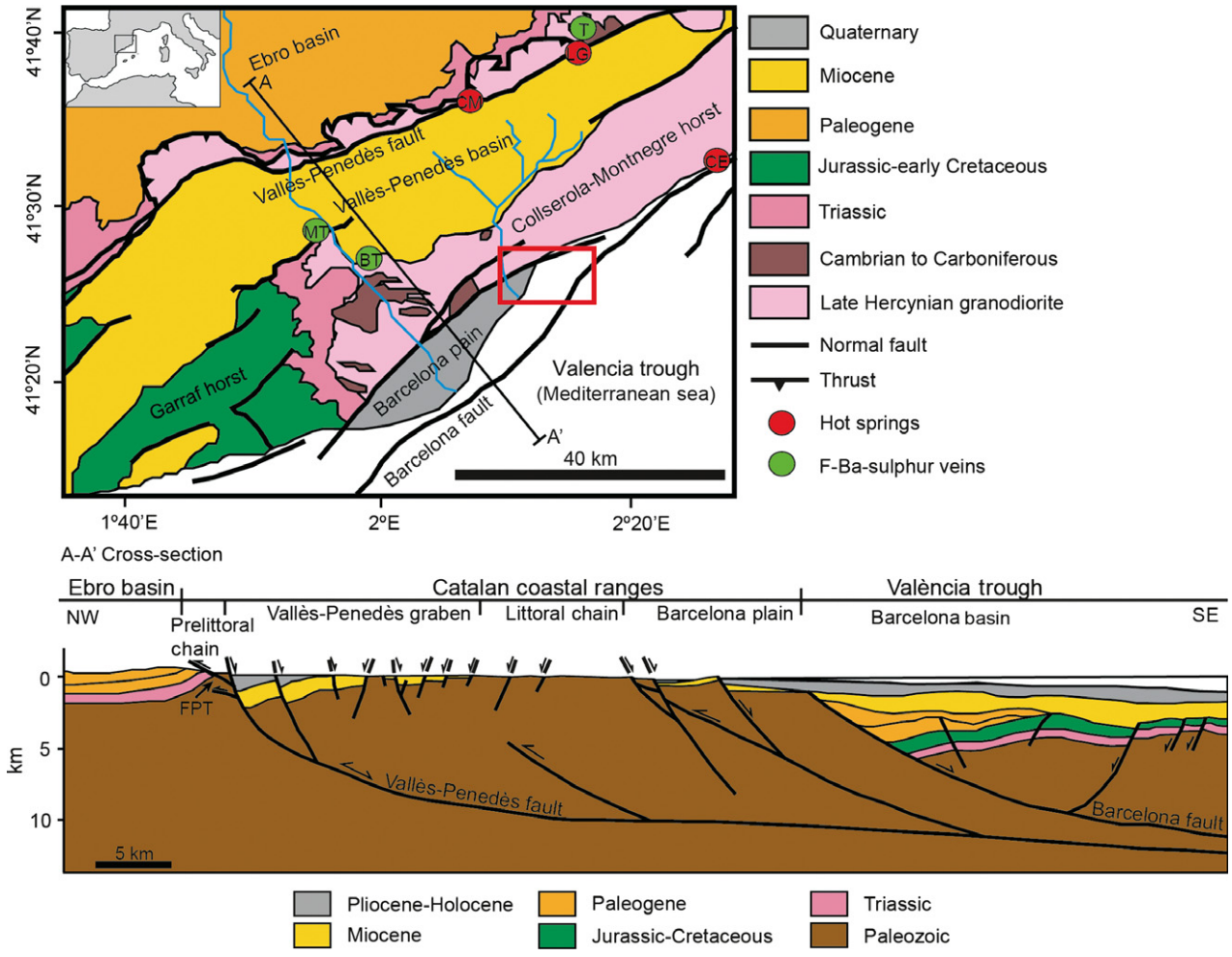

Fig. 1. Schematic geological map of the Catalan Coastal Ranges with localization of the studied area and cross section (Santanach *et al.* 2011). T, Tagamanent; MT, Martorell; BT, Berta Mine; CM, Caldes de Montbui; LG, La Garriga; CE, Caldes d'Estrac.

Horst, which is mainly formed by Paleozoic rocks consisting of Cambro-Ordovician shales and phyllites, Silurian black shales and phyllites, Devonian carbonates, Carboniferous Culm facies and late Hercynian leucogranites, tonalites and granodiorites (Julivert & Durán 1990). In this horst, the Mesozoic cover has been almost completely eroded.

The present study concerns the NE-SW segmented fault that defines the northern boundary of the Barcelona Plain in its northeastern sector, the Hospital fault. This fault juxtaposes Triassic rocks in the north and Miocene rocks in the south against the basement granodiorite, and it is crosscut by an orthogonal fault system (Fig. 2).

METHODS AND ANALYTICAL TECHNIQUES

Fifty-two samples were collected from the outcrops, and two samples of the unaltered granodiorite were obtained from boreholes. Thirty of these samples are from the fault core between the late Hercynian granodiorite and the Triassic rocks, twenty samples are from faults affecting middle Triassic dolostones, and two are from the fault core between the Triassic and Silurian rocks. Thirty-nine thin sections were studied using optical and cathodoluminescence microscopes. Some of the thin sections were stained with Alizarine Red-S and potassium ferricyanide to distinguish calcite and dolomite and their ferroan equivalents (Dickson 1966). A Technosyn Cold Cathodoluminescence Model 8200 MkII operating at 16–19 kV and 350 μA gun current was used. Some thin sections were also examined under ESEM Quanta 200 FEI, XTE 325/D8395 scanning electronic microscope.

X-ray diffraction of bulk rock and oriented aggregates have been performed with a Bragg-Brentano PAnalytical X'Pert PRO MPD alpha 1 operating at 1.5406 A, 45 kV and 40 mA.

After the petrographic study, carbon-coated thin sections were used for elemental analyses of carbonate cements with

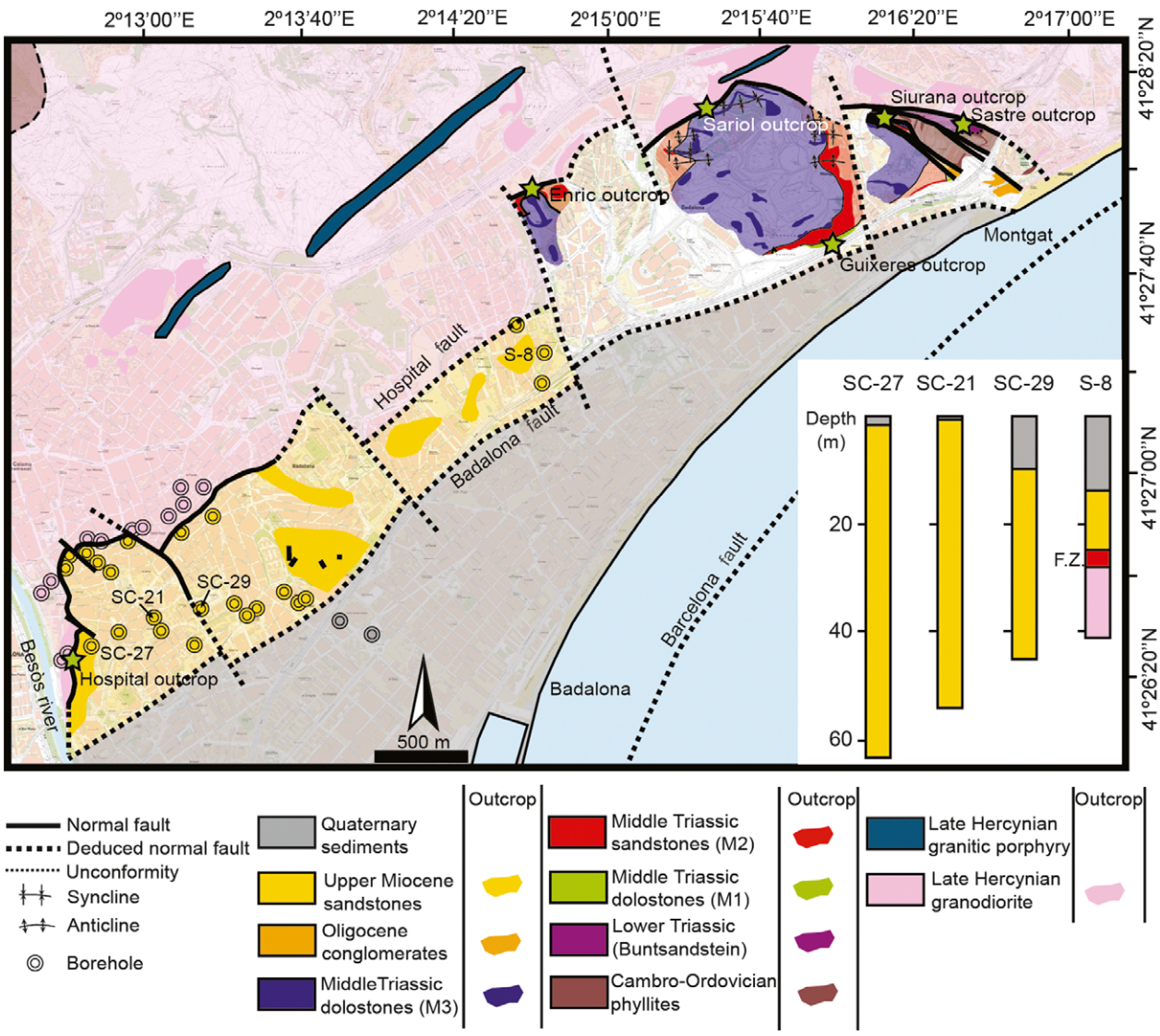

Fig. 2. Detailed geological map of the northern sector of the Barcelona Plain with outcrop and borehole locations. Schematic columns of four of the boreholes are shown. F.Z., fault zone.

a CAMECA model SX-50 microprobe. It was operated using 15 nA of current intensity, 20 kV of acceleration voltage, and a beam diameter of 10 μm. The detection limits are 99 ppm for Na, 312 ppm for Ca, 436 ppm for Mg, 149 ppm for Fe, 107 ppm for Mn, and 124 ppm for Sr. The precision of major elements is about 0.64% (at 2σ level).

Sixty-eight microsamples for carbon and oxygen stable isotopes were powdered with a microdrill. Collected samples were reacted with 100% phosphoric acid at 70°C for two minutes in an automated Kiel Carbonate Device attached to a Thermal Ionization Mass Spectrometer Thermo Electron (Finnigan) MAT-252. The results are expressed in δ VPDB standard. Standard deviation is ±0.02 for $\delta^{13}C$ and ±0.05 for $\delta^{18}O$. Cements C6 and D3 could not be sampled due to the micrometric thickness of fractures and their spatial relationship with other carbonatic cements.

LITHOLOGY AND PETROGRAPHY OF THE HOST ROCKS

The granodiorite shows a phaneritic and granular texture. The grain size is mostly about 2–3 mm, but there are feldspars around 5 mm. It is constituted by quartz, potassic feldspar, plagioclase, and biotite (<5%). The potassic feldspar, identified as orthose, has perthites and is partially replaced by kaolinite. Some of them are poikilitic. The plagioclase shows polysynthetic twins, and it is partially altered to sericite. Finally, the biotite has some interlayered epidote and shows a very incipient alteration to chlorite.

Silurian rocks consist on phyllites and clay-rich black shales. Phyllites are only present as clasts in fault-related breccias. The Silurian black shales are constituted by phyllosilicates, quartz, calcite, potassic feldspar, plagioclase, jarosite (oxidation of iron sulfides), and hematites. Specifically, the phyllosilicates are 65% illite, 10% chlorite, and 25% illite-smectite.

Middle Triassic rocks are represented by Muschelkalk facies M1, M2, and M3. The Muschelkalk facies M2 is formed by lutites and layers of sandstones. Lutites are formed by quartz, calcite, potassic feldspar, plagioclase, and clays (65% illite, 20% illite-smectite, 10% chlorite-smectite, and 5% chlorite). The red sandstones are constituted by quartz, potassic feldspar, plagioclase, muscovite, and biotite. Grains are 160 μm in size and are cemented by orange luminescent calcite.

Muschelkalk facies M1 and M3 are formed by dolostones which consist of 2- to 50-cm-thick beds that form NE-SW-oriented folds. Four different types of dolostones have been identified: host rocks HR1 and HR2 in the M1 and HR3 and HR4 in the M3. HR1 dolostone is constituted by clear anhedral crystals about 50 μm thick and euhedral crystals with a cloudy nucleus and clear borders about 250 μm thick. HR1 shows a brown-yellowish luminescence. HR2 consists of an orange luminescent dolmicrite. HR3 dolostone is constituted of anhedral crystals about 80 μm and euhedral crystals about 180 μm in size with a cloudy nucleus and dull red luminescence. Ghosts of coated grains indicate that the replaced rock was at least locally a grainstone and that dolomitization was nondestructive. Finally, HR4 is formed by anhedral crystals about 60 μm in size with an orange dull luminescence. The dolostones have $\delta^{18}O$ values between −4.6 and −2.7 vPDB and $\delta^{13}C$ values between +0.7 and +2.8 vPDB. With regard to their elemental geochemistry, HR3 shows higher contents in Mn and Fe and lower contents in Sr than the other host rocks (Table 1). HR4 have contents of Na and Sr below the analytical detection limit. The dolostones of M1 are partially replaced by a clear anhedral dolomite with dull red luminescence (replacive dolomite RD1).

Finally, the Miocene rocks are represented by matrix supported and heterometric conglomerates. Clasts range from cobble to granule and are mainly derived from the Paleozoic basement although some clasts of the Triassic rocks are identified. The most abundant lithologies are phyllites (40%) and quartzites (35%) followed by knotted hornfels (10%), quartz grains derived from quartzites and granodiorites (7%), porphyries (4%), granodiorite (1%), Muschelkalk (2%), and Buntsandstein (1%) clasts. Clasts are usually angular except phyllites and knotted hornfels, which are rounded. The matrix is formed by red shales and silts. The sand-sized grains include angular quartz and subrounded orthose. The smaller matrix fraction includes quartz, potassium feldspar, illite, chlorite, kaolinite, mixed-layer of illite-chlorite, apatite, iron oxides, and titanium oxides. Cretaceous clasts are absent.

FRACTURE SETS ANALYSIS

Nine generations of fractures have been identified in the studied area and have been arranged in chronological order according to their crosscutting relationships (Fig. 3).

The first three generations have been attributed to the first tectonic event, which is characterized by extensional axes from ENE-WSW to WNW-ESE direction. Type-1A fractures have only developed in the Triassic dolostones of the hanging-wall of the Hospital fault, and they are represented by NE-SW normal faults with dip about 49°SE and by NW-SE normal faults with a certain right-lateral component with dip from 60 to 90° to the SW and NE. Type-1B fractures are normal faults with NE-SW trending and dip between 24 and 67° to the SE. In the Hospital outcrop, slickenlines with 14/076 orientation indicate a certain left-lateral motion during normal faulting. Although the similar orientation of 1A and 1B faults, the study of their cements demonstrated their activity during different stages.

The second tectonic event shows NNE-SSW compressional axes. It is constituted by type-2 fractures that are reverse faults with NE-SW trend and dip toward the SE, which have a strong left-lateral component. This faulting episode is the responsible of the formation of the NE-SW-oriented folds in the Muschelkalk units. Minor faults of this group affecting Triassic rocks of the horst reactivate previous 1A faults.

The third tectonic event has variable extensional axes from NNW-SSE to NE-SW and is represented by five generations of fractures. Type-3A fractures are the most abundant in the Barcelona Plain. They are from NE-SW to E-W striking normal faults with a steep dip, mostly, to the SE. The second generation, type-3B fractures, is made of joints with a WNW-ESE trend and elevated dip to the NE, whereas type-3C fractures are NE-SW seams with low dip to the NW. The fourth generation, type-3D, is represented by a set of mainly oriented N-S normal faults dipping from 30 to 80° to the east and barely to the SW and NE-SW normal faults that are the reactivation of previous 3A and 2 faults. Type-3E fractures are open joints with NW-SE trend and dip about 60° to the SW that result from the opening of previous 1A faults. Finally, type-3F strike-slip faults formed and offset previous type-3A main normal faults. These faults, however, do not crop out in the Barcelona Plain but are deduced from regional mapping.

FAULT ZONES: STRUCTURE, MICROSTRUCTURES, AND CHEMISTRY

This section has been divided in two parts: the Hospital fault and the horst between the Hospital and the Badalona faults (or Hospital hanging-wall).

Table 1 Elemental geochemistry and $\delta^{18}O$-$\delta^{13}C$ composition of the carbonate cements and host rocks.

		Ca (ppm)	Mg (ppm)	Na (ppm)	Mn (ppm)	Fe (ppm)	Sr (ppm)	$\delta^{18}O$ (VPDB)	$\delta^{13}C$ (VPDB)
Hospital fault cements									
C1a (n = 10)	Min	391 591	<d.l.	<d.l.	1681	<d.l.	968	−15.6	−6.5
	Max	396 633	<d.l.	241	4425	326	1342	−15.0	−6.3
	Average	393 805	<d.l.	<d.l.	2937	<d.l.	1218	−15.4	−6.4
C1b (n = 1)	Min	–	–	–	–	–	–	–	–
	Max	396 148	<d.l.	5302	<d.l.	2983	1044	–	–
	Average	–	–	–	–	–	–	–	–
C1c (n = 53)	Min	387 038	<d.l.	<d.l.	190	<d.l.	293	–	–
	Max	403 308	1049	366	5031	1078	1687	–	–
	Average	396 219	<d.l.	131	1074	137	1340	–	–
C1d (n = 8)	Min	386 130	<d.l.	<d.l.	<d.l.	<d.l.	1141	–	–
	Max	395 492	1367	<d.l.	3537	1034	1580	–	–
	Average	391 541	<d.l.	<d.l.	2305	507	1410	–	–
C1e (n = 7)	Min	391 093	<d.l.	<d.l.	594	<d.l.	1212	–	–
	Max	402 147	2260	236	2120	734	1867	–	–
	Average	394 577	<d.l.	<d.l.	1308	387	1437	–	–
C1f (n = 11)	Min	390 100	<d.l.	<d.l.	<d.l.	<d.l.	158	−16.4	−6.2
	Max	414 500	<d.l.	1906	640	917	480	−16.2	−5.9
	Average	403 055	<d.l.	419	<d.l.	248	357	−16.3	−6.1
C1 (n = 11)	Min	385 500	<d.l.	<d.l.	<d.l.	<d.l.	251	–	–
	Max	411 300	4980	216	1160	610	590	–	–
	Average	400 636	811	107	827	260	467	−15.1	−6.9
C2a (n = 47)	Min	384 720	<d.l.	<d.l.	<d.l.	<d.l.	971	−5.5	−7.1
	Max	400 837	2990	362	7168	6250	1880	−4.6	−6.5
	Average	390 998	873	<d.l.	3031	1188	1378	−5.0	−6.9
C2b (n = 7)	Min	386 100	<d.l.	<d.l.	1086	<d.l.	157	–	–
	Max	400 200	1430	<d.l.	5629	1064	464	–	–
	Average	392 286	671	<d.l.	3366	633	319	−5.8	−7.2
C2c (n = 10)	Min	397 800	<d.l.	<d.l.	232	<d.l.	198		
	Max	405 600	<d.l.	<d.l.	770	233	445		
	Average	401 610	<d.l.	<d.l.	459	<d.l.	309		
C3a (n = 38)	Min	396 200	<d.l.	<d.l.	641	<d.l.	309	−20.8	−6.2
	Max	409 300	<d.l.	197	2299	313	610	−19.6	−6.1
	Average	401 982	<d.l.	<d.l.	1102	<d.l.	460	−20.2	−6.2
C3b (n = 15)	Min	392 100	<d.l.	<d.l.	925	<d.l.	<d.l.	–	–
	Max	410 400	<d.l.	330	6445	6576	879	–	–
	Average	402 020	<d.l.	123	2161	686	486	−18.4	−6.1
C4 (n = 20)	Min	378 100	<d.l.	<d.l.	<d.l.	<d.l.	195	–	–
	Max	407 200	9265	230	5421	2475	714	–	–
	Average	390 495	2981	<d.l.	1766	844	479	−5.8	−7.7
C5 (n = 8)	Min	209 200	761	<d.l.	<d.l.	576	278	−2.9	−7.6
	Max	388 600	104 973	<d.l.	4401	8698	1429	−2.6	−7.6
	Average	311 650	47 549	<d.l.	1510	217	786	−2.8	−7.6
C6 (n = 7)	Min	340 200	<d.l.	<d.l.	<d.l.	<d.l.	<d.l.	–	–
	Max	406 800	39 585	336	2381	593	1599	–	–
	Average	373 771	18 928	139	537	275	925	–	–
C7 (n = 22)	Min	360 100	11 294	<d.l.	<d.l.	<d.l.	179	−2.9	−8.5
	Max	384 800	29 628	355	1573	1066	1271	−2.5	−8.3
	Average	374 086	19 127	<d.l.	130	402	750	−2.8	−8.4
PC1a (n = 13)	Min	225 900	<d.l.	<d.l.	<d.l.	<d.l.	<d.l.	−2.7	−7.8
	Max	395 300	121 058	<d.l.	6644	2764	1019	−1.9	−7.7
	Average	311 385	59 794	<d.l.	1043	834	533	−2.3	−7.7
PC1b (n = 10)	Min	383 400	<d.l.	<d.l.	3713	771	<d.l.		–
	Max	392 000	1123	<d.l.	7766	4351	385		–
	Average	387 450	509	<d.l.	5634	1567	262		–
Hnaging-wall cements									
HR1 (n = 15)	Min	211 248	128 308	<d.l.	<d.l.	<d.l.	376	−4.6	+0.7
	Max	219 995	152 760	454	160	1269	700	−3.4	+2.6
	Average	216 260	133 803	287	<d.l.	431	556	−3.9	+1.8
HR2 (n = 22)	Min	202 598	121 744	107	<d.l.	<d.l.	<d.l.	−3.3	+0.9
	Max	222 716	132 719	354	188	17 845	857	−2.7	+2.3
	Average	217 949	129 416	248	<d.l.	1686	532	−3.0	+1.6
HR3 (n = 21)	Min	213 966	104 916	<d.l.	<d.l.	597	271	−3.7	+2.6
	Max	245 753	135 569	517	960	3844	564	−3.5	+2.8
	Average	219 847	126 945	191	321	1472	437	−3.6	+2.7

Table 1 (Continued).

		Ca (ppm)	Mg (ppm)	Na (ppm)	Mn (ppm)	Fe (ppm)	Sr (ppm)	$\delta^{18}O$ (VPDB)	$\delta^{13}C$ (VPDB)
HR4 (*n* = 15)	Min	215 966	126 808	<d.l.	<d.l.	741	<d.l.	–	–
	Max	221 039	131 053	<d.l.	398	3164	<d.l.	–	–
	Average	218 155	128 749	<d.l.	222	1678	<d.l.	–	–
RD1 (*n* = 15)	Min	216 438	128 123	<d.l.	<d.l.	<d.l.	248	–	–
	Max	222 747	136 806	209	205	1466	610	–	–
	Average	219 484	131 651	<d.l.	<d.l.	557	395	–	–
D1 (*n* = 36)	Min	213 612	127 591	<d.l.	<d.l.	<d.l.	<d.l.	−5.9	+2.3
	Max	221 864	134 565	470	201	1800	800	−5.4	+2.4
	Average	218 295	130 251	185	<d.l.	604	563	−5.6	+2.4
D2a (*n* = 18)	Min	214 197	123 803	<d.l.	<d.l.	<d.l.	<d.l.	−7.2	+2.5
	Max	223 924	131 800	351	177	870	681	−6.8	+2.6
	Average	218 926	128 898	181	<d.l.	440	468	−7.0	+2.6
D2b (*n* = 13)	Min	216 494	121 831	<d.l.	<d.l.	424	<d.l.	–	–
	Max	221 205	132 860	230	799	7803	555	–	–
	Average	218 862	129 130	118	187	2813	349	–	–
D3 (*n* = 23)	Min	210 900	126 284	<d.l.	<d.l.	400	448	–	–
	Max	224 411	132 600	200	200	1500	900	–	–
	Average	218 303	129 328	<d.l.	<d.l.	878	640	–	–
CD1 (*n* = 15)	Min	389 200	<d.l.	<d.l.	<d.l.	<d.l.	1300	−5.9	−7.4
	Max	395 100	2300	300	400	700	2100	−4.9	−5.4
	Average	392 793	1053	<d.l.	160	340	1740	−5.3	−6.3
CD2 (*n* = 14)	Min	392 600	700	<d.l.	<d.l.	<d.l.	700		–
	Max	404 400	2900	300	200	300	2000		–
	Average	396 757	1250	<d.l.	<d.l.	<d.l.	1500		–
CD3 (*n* = 88)	Min	390 000	<d.l.	<d.l.	<d.l.	<d.l.	700		–
	Max	404 800	1900	300	2200	1100	2200		–
	Average	398 092	928	<d.l.	<d.l.	<d.l.	1417		–
CD4 (*n* = 18)	Min	389 800	600	<d.l.	<d.l.	<d.l.	1200		–
	Max	398 500	2700	200	<d.l.	800	1700		–
	Average	394 150	1139	<d.l.	<d.l.	244	1444		–
Calcitized dolostone	Min	–	–	–	–	–	–	−9.5	−4.8
	Max	–	–	–	–	–	–	−4.1	−3.2
	Average	–	–	–	–	–	–	−7.6	−4.2
Dolomite speleoth (*n* = 2)	Min	236 600	102 900	400	<d.l.	<d.l.	2300	–	–
	Max	250 300	110 600	500	<d.l.	<d.l.	3700	–	–
	Average	243 450	106 750	450	<d.l.	<d.l.	3000	−2.6	−9.3
High-Mg calcite sp. (*n* = 17)	Min	360 400	8800	<d.l.	<d.l.	<d.l.	5300	−5.3	−9.8
	Max	385 800	24 900	600	200	<d.l.	13 800	−4.7	−8.5
	Average	375 176	16 976	282	<d.l.	<d.l.	7506	−4.9	−9.4
Calcite speleoth. (*n* = 4)	Min	388 000	3500	<d.l.	<d.l.	<d.l.	2200	–	–
	Max	398 700	6700	300	<d.l.	<d.l.	2600	–	–
	Average	393 800	4400	<d.l.	<d.l.	<d.l.	2425	–	–
Aragonite speleoth. (*n* = 6)	Min	389 300	<d.l.	<d.l.	<d.l.	<d.l.	4800	−4.6	−9.8
	Max	395 800	<d.l.	500	<d.l.	<d.l.	8200	−4.2	−9.2
	Average	392 517	<d.l.	283	<d.l.	<d.l.	6783	−4.4	−9.4
High-Mg rafts (*n* = 8)	Min	308 600	25 800	600	<d.l.	<d.l.	2200	−4.6	−9.0
	Max	357 400	64 300	1400	200	300	3300	−3.3	−8.2
	Average	335 538	43 688	950	<d.l.	<d.l.	2650	−3.8	−8.6

<d.l.: below the analytical detection limit.
n: number of elemental analysis spots.

The Hospital fault

The Hospital fault is a NE-SW fault zone with increasing dip toward the northeast from 29 to 63°SE. It shows in its northern ending a splay structure as a result of thrusting with a left-lateral component and later N-S extension (Fig. 2). This fault separates the late Hercynian granodiorite from the Triassic rocks. To describe the deformation along this main fault zone, we have studied three outcrops settled at different segments of the fault. In the Hospital and Enric outcrops, the granodiorite is in tectonic contact with the M2 unit, whereas in the Sariol, outcrop is in tectonic contact with the M3 unit.

The Hospital outcrop

The fault zone architecture in this segment of the Hospital fault is very complex due to the concentration of the three tectonic events in a reduced area (~20 m) (Fig. 4A,B). The first tectonic event is represented by type-1B faults. One of these faults juxtaposes the Middle Triassic clays and sandstones against the late Hercynian granodiorite. This major normal fault has low dip (about 30°SE) and generates a

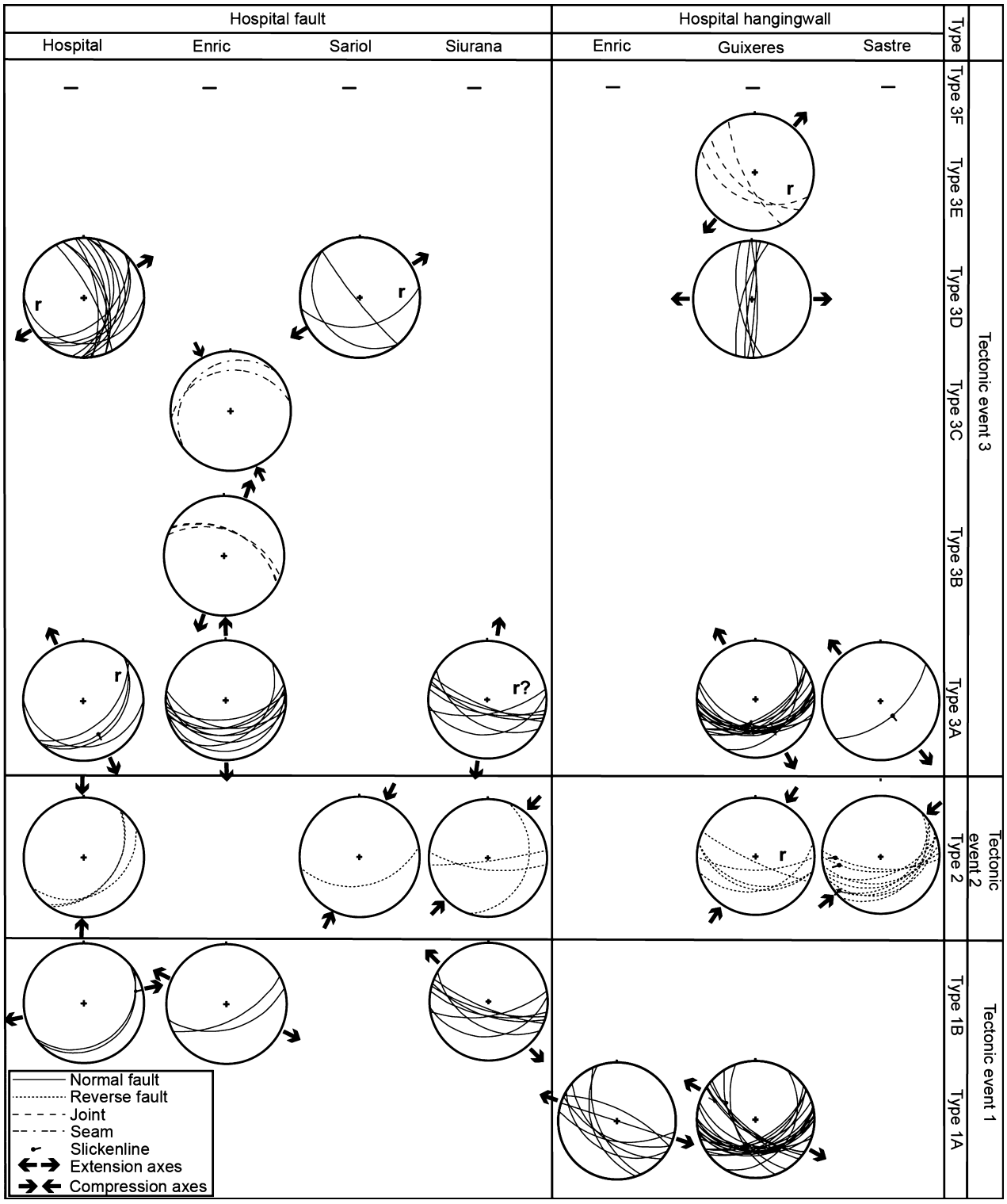

Fig. 3. Stereoplots of the different generations of fractures in Schmidt lower hemisphere projections with strain directions. The 'r' marks reactivated fractures.

core zone about 70 cm width (FC1) with well-defined and sharp boundaries. The core is formed by 60 cm of a cataclastic green material and by 10 cm of a discontinuous foliated red and black clay gouge (Fig. 4C,D). Also, compressive type-2 faults are present and develop two decimetric-scale duplexes in the hanging-wall that locates the

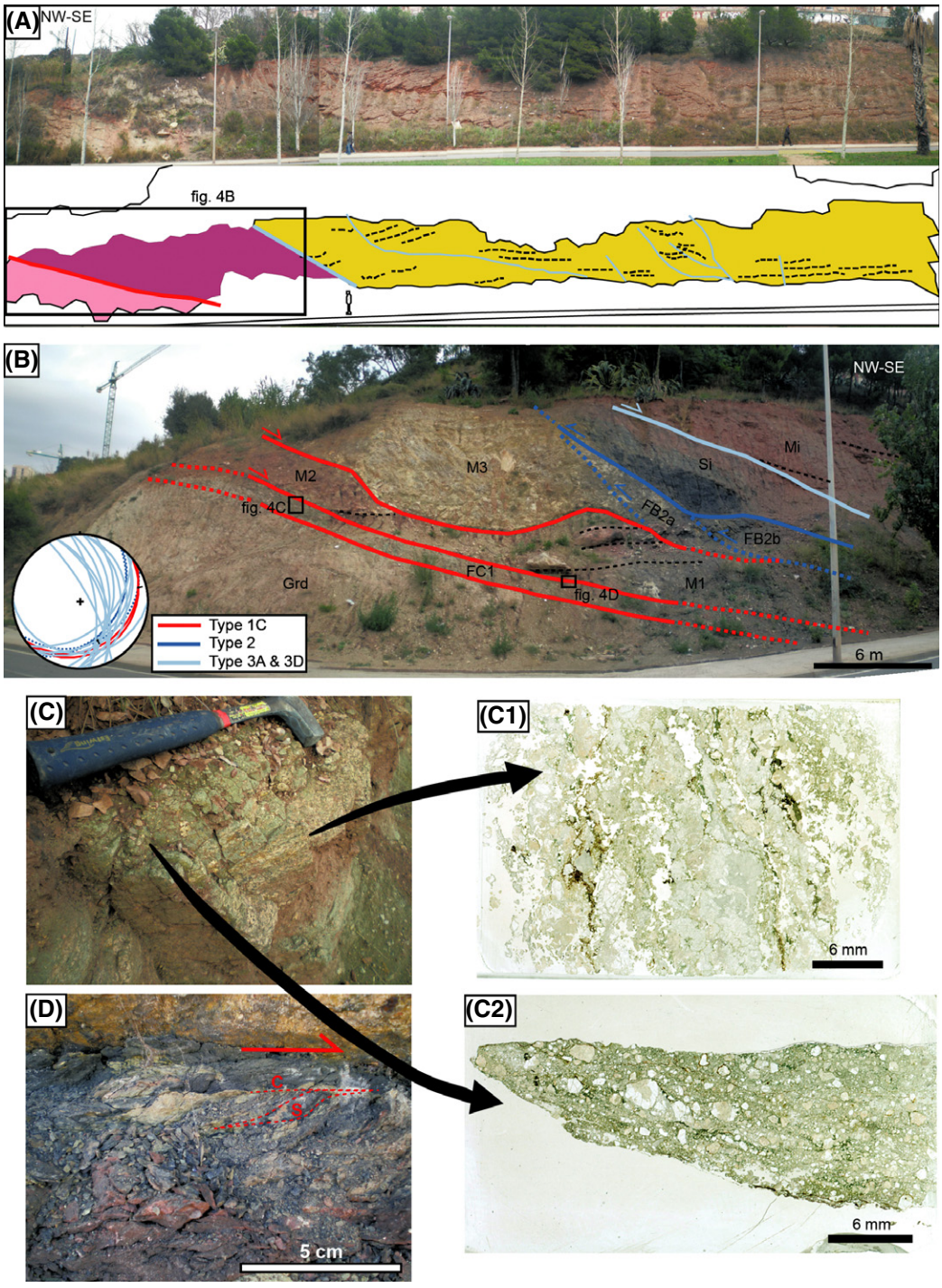

Fig. 4. Hospital outcrop. (A) General view of the Hospital outcrop. Legend: pink: granodiorite; purple: deformation zone formed by Triassic and Silurian rocks; yellow: Miocene conglomerates. Faults are in red and bedding in black. (B) Enlarged area marked in A, where most of deformation is concentrated, and stereoplot of the sets of fractures. Legend: Grd: granodiorite; Si: Silurian; M1: Lower Muschelkalk dolostones; M2: Middle Muschelkalk clays and sandstones; M3: Upper Muschelkalk dolostones; Mi: Miocene conglomerates; FC1: fault core 1; FB2a: fault breccias with carbonate clasts; FB2b: fault breccias with phyllite clasts. (C) Photograph of the cataclastic green band of the fault core FC1. Observe the different degrees of comminution: (C1) Thin section of the breccia. (C2) Thin section of the slightly foliated cataclasite. (D) Foliated red and black gouge of the fault core FC1.

Silurian phyllites on top of the Middle Triassic dolostones (Fig. 4B). Each duplex is constituted by different breccias. Breccia FB2a is constituted by dolomitic clasts from the Triassic unit M3, whereas breccia FB2b contains clasts of the Silurian phyllites. Finally, a type-3D extensional fault, reactivation of a previous 3A fault, settles the Miocene in

contact with the Silurian black shales. The Silurian acts as a detachment level and accommodates all the deformation. In the Miocene conglomerates, minor type-3D normal faults are present. These minor faults do not develop fault cores in this outcrop.

The study is centered in the analysis of the fault core FC1. The cataclastic band resulting from granodiorite deformation shows that the type-1B fault was successively reactivated generating different fault rocks and cements.

During a first stage, took place the precipitation in geodes of euhedral quartz crystals, up to 1 mm in size, with concentric bands of fluid inclusions, the overgrowth of albites and the precipitation of orthose in mode I fractures up to 50 μm wide affecting the feldspars. Moreover, orthose was more altered to kaolinite and albite to sericite in the deformed granodiorite.

During a second stage, a dilatant random breccia was formed and cemented by five calcite cements C1 (Fig. 5A–D). Cement C1a is constituted by twinned bright orange luminescent calcite filling vugs and mode I fractures (opening). Crystal size is 1–2 mm, $\delta^{18}O$ values range between −15.6 and −15.0 vPDB and $\delta^{13}C$ values between −6.5 and −6.3 vPDB. Cement C1b, which fills fractures in cement C1a, is only visible under the cathodeluminescence microscope by its dark brown luminescence. It shows high values of Na and Fe, averaging 5302 and 2983 ppm, respectively. Cement C1c is constituted by twinned sparitic brownish-orange luminescent calcite. This cement has crystals up to 1 mm when cementing mode I fractures and mode II fractures (sliding), where it is syn-kynematic, and crystals about 100 μm when cementing small patches of cataclasite inside the dilatant breccia. Cement C1d is formed by euhedric orange luminescent calcite crystals smaller than 50 μm that fills mode I fractures. Finally, cement C1e is constituted by euhedric brownish-orange luminescent calcite, 125 μm in size, that fills mode I fractures. The detailed elemental geochemistry of all these calcite cements is summarized in Table 1.

Later, the previously formed dilatant breccia was further deformed as a slightly foliated cataclasite is constituted by reworked clasts of both the granodioritic host rock and the dilatant breccia. The foliation is oblique to the main fault plane and indicates the normal slip of the fault (Fig. 4C2). It is constituted by calcite cement C1f, iron oxides and chlorites (Fig. 5E). The cement C1f is constituted by twinned brownish-orange luminescent sparitic calcite about 100 μm. $\delta^{18}O$ and $\delta^{13}C$ values are nearly constant about −16.3 vPDB and −6.0 vPDB, respectively. Unlike the previous cements, C1f calcite has Mn values below the detection limit and lower values of Sr, about 357 ppm (Table 1). The iron oxides occur in the cataclasite matrix defining the foliation and also form envelops around the reworked clasts of the cataclasite (Fig. 4C2). Chlorites are both detrital and neoformed as patches growing within the cataclastic matrix.

The red and black clay gouge has an S-C fabric consistent with a normal slip (Fig. 4D). It is made up of quartz, calcite, potassic feldspar, plagioclase, anhydrite, and clays. Clays constitute between 45% and 55% of the fault rock of which 65% is illite, 5% chlorite, 20% illite-smectite, and 10% chlorite-smectite. This clay composition is similar than in the lutites of the M2 unit, indicating that this gouge represents the deformation of the hanging-wall coeval to the generation of the green cataclastic band.

During the last stage, vug porosity within the dilatant breccia and mode I fractures of the Triassic sandstones of the hanging-wall were cemented by cement C2a. This cement is constituted by anhedral calcite crystals between 100 and 500 μm in size with a zoned orange and brown luminescence (Fig. 5B,F). It has Mn values up to 7168 ppm and Fe values up to 6250 ppm. The $\delta^{18}O$ values of C2a range between −5.5 and −4.6 vPDB and the $\delta^{13}C$ between −7.2 and −6.5 vPDB.

The Enric outcrop

The Hospital fault in this outcrop dips 55° toward the SE. At outcrop scale two fault rocks are recognized: a first generation of a 2-m-thick dark-green cohesive breccia with irregular boundaries and a later 20-cm-thick greenish-yellow semicohesive gouge with sharp and well-delimited boundaries (Fig. 6A). Both fault rocks resulted from the brittle deformation of the granodiorite. Five sets of fractures were measured in the cohesive breccias (Fig. 6B).

The dark-green cohesive breccia was formed from several stages of deformation. Deformation began with the development of a random cataclastic breccia, which microfractures were cemented by epidotes (clinozoisites and epidotes s.s.) and chlorites (Fig. 7A). Some of the clasts of this breccia are of mylonite, indicating a previous deformation stage within the ductile regime. Quartz and feldspar recrystallization of the mylonite was mainly produced by bulging and some subgrain rotation. Affecting this breccia, multiepisodic pull-aparts were formed in type-1B faults of little slip. These pull-aparts are cemented by calcite C1 (Fig. 7B). The cement is formed by anhedral to euhedral bright orange luminescent calcite crystals up to 30 μm in size. Geochemically, this cement has higher Mg content than the cements C1 of the Hospital outcrop (Table 1). It has a $\delta^{18}O$ value of −15.1 vPDB and a $\delta^{13}C$ value of −6.9 vPDB.

Later, the development of pseudotachylytes took place in type-3A normal faults (Fig. 7C), which usually show bifurcations (Fig. 6B). They form very thin fault veins and injection veins. Pseudotachylyte fault veins have a width up to 125 μm and have sharp and straight walls. Under transmitted light, pseudotachylytes display yellow-brownish colors, whereas under polarized light, they show a dark

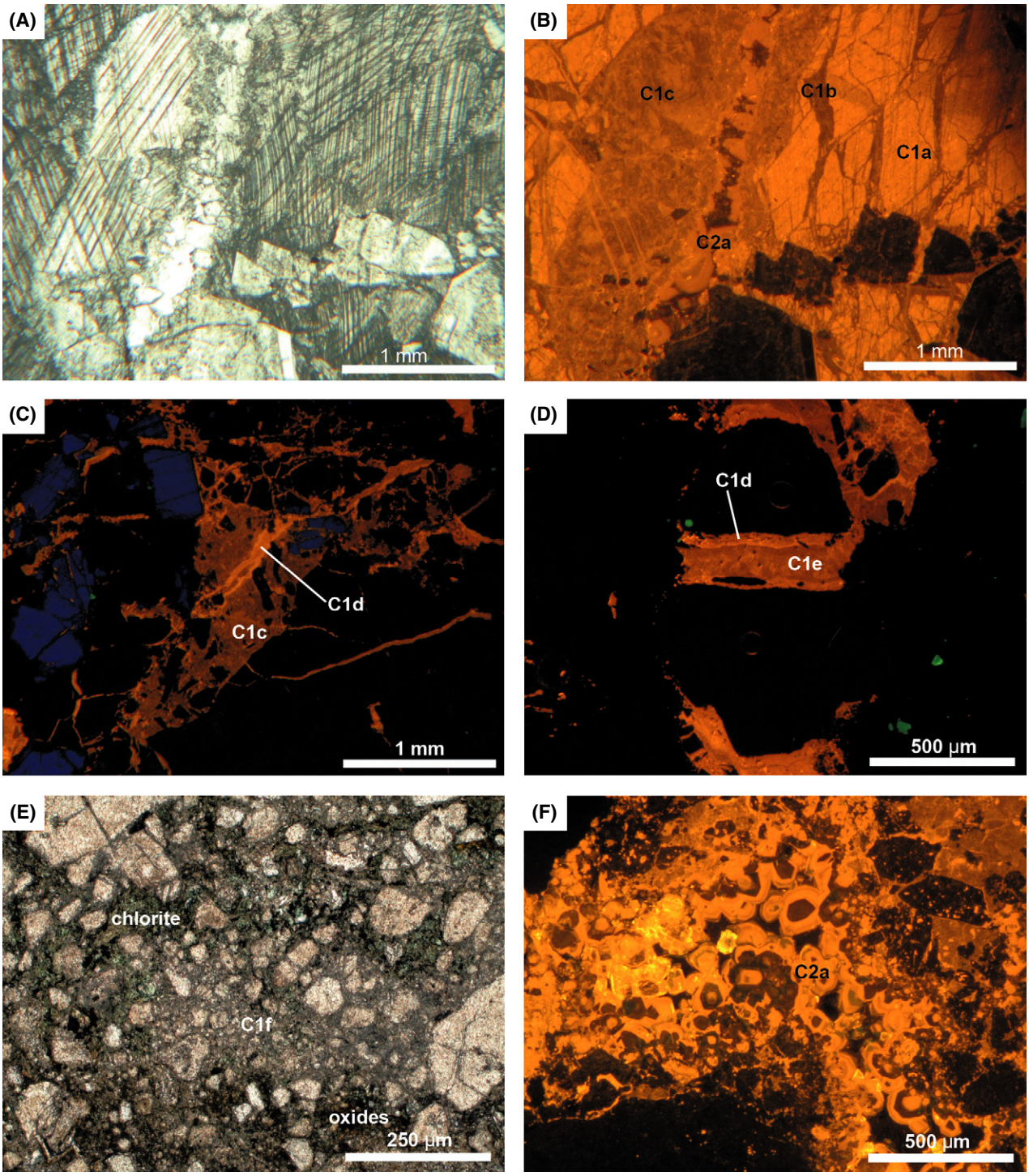

Fig. 5. Microphotographs of the minerals cementing the Hospital fault rocks in the Hospital outcrop. (A, B) Plane polarized light and cathodoluminescence images of calcite cements C1a,b,c and later C2a. (C) Cathodoluminescence of calcite cements C1c, which cements patchy cataclasites, and C1d. (D) Image of cathodoluminescence of calcites C1d and C1e. (E) Plane polarized light image of the cataclasite. Observe the three neoformed minerals linked to this fault rock: chlorite, calcite C1f, and iron oxides. (F) Vug porosity infilled by the zoned cement C2a in the cataclastic band (cathodoluminescence).

aphanitic matrix that contain subrounded clasts of quartz and feldspar. The study under the optical microscope points to the devitrification of the matrix. The discontinuities generated by these fault rocks were later profit for crack-seal veins to develop (Fig. 7C). These crack-seals have internal shear planes and produce the reorientation in localized zones of the previously formed cataclastic breccia. The result is the generation of a cataclasite with foliated

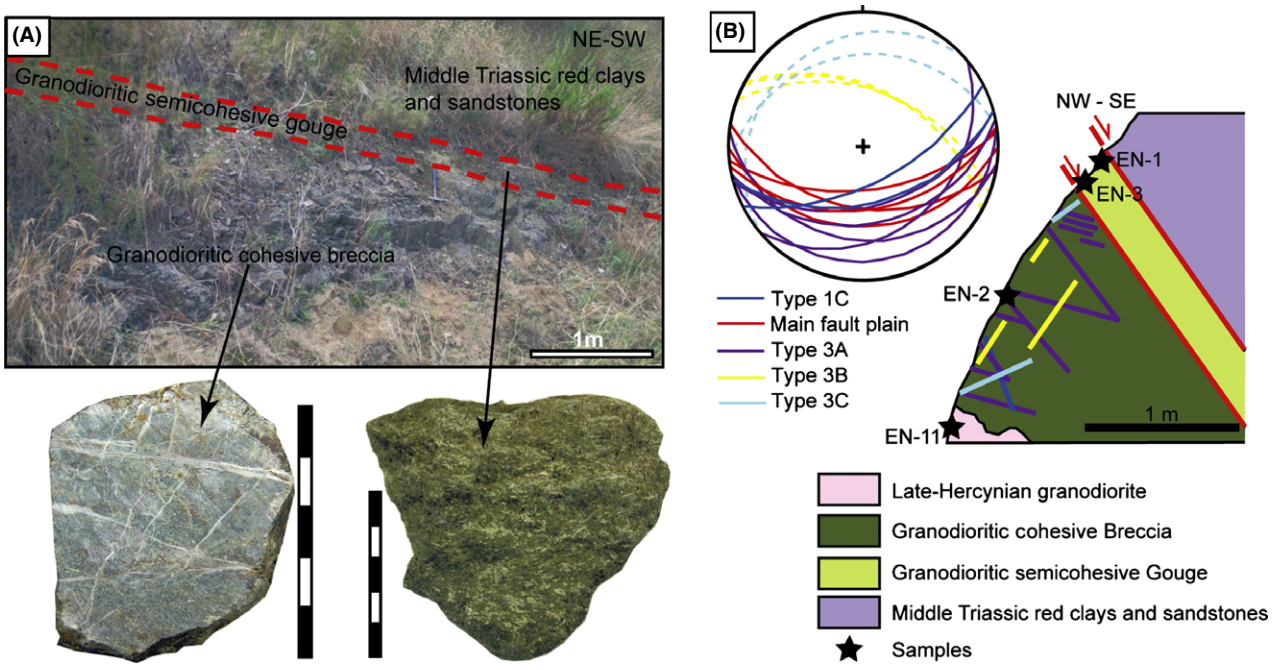

Fig. 6. Enric outcrop. (A) Poorly outcropping of the Hospital fault in the Enric outcrop and hand samples of the cohesive breccia and semicohesive gouge. Each bar subdivision is 1 cm. (B) Synthetic cross section of the fault zone, with sample location and projection of the identified sets of fractures.

fabric marked by planes of oxides, chlorites, and epidotes. The crack-seals are cemented by the calcite cement C3a, which is a twinned anhedral to euhedral sparry calcite, from micrite to 200 μm in size, with a bright orange luminescence (Fig. 7C,D). It is characterized by $\delta^{18}O$ values between −20.8 and −19.6 vPDB and $\delta^{13}C$ values about −6.2 vPDB. The next stage generated the development of type-3B joints, which are cemented by calcite C3b. This calcite is formed by anhedral crystals up to 30 μm in size, in which bright orange luminescence increases toward the borders (Fig. 7D). This increase in luminescence is also reflected in the increase in Mn content, up to 6445 ppm. Its $\delta^{18}O$ value is −18.4 vPDB and its $\delta^{13}C$ value is −6.1 vPDB. Finally, 3C seams of iron oxides were formed.

The greenish-yellow semicohesive gouge, generated in type-3A normal faults, is constituted by smectite, chlorite, and illite and results from a completely comminution and alteration of the original granodiorite. The gouge is affected by mode I fractures filled by cement C4 (Fig. 7E). Cement C4 consists of microsparite calcite crystals with bright orange luminescence that shows a $\delta^{18}O$ value of −5.8 vPDB and a $\delta^{13}C$ value of −7.7 vPDB. This cement also has Mg content up to 9265 ppm (2981 ppm in average).

After all the mentioned deformation events, a soil developed in the gouge, giving cohesivity to the fault rock. Two cements are recognized: cement C6 consists of micritic orange luminescent high-Mg calcite crystals that form nodules between 1 mm and 1 cm of diameter that include fragments of quartz and feldspar; cement C7 is constituted by anhedral sparitic nonluminescent high-Mg calcite crystals up to 30 μm in size that forms a centimetric carbonate level that contains the nodules of cement C6. Crystals show spherulitic and 'corn-cob' arrangements (Fig. 7E,F). This cement has $\delta^{18}O$ values between −2.9 and −2.5 vPDB and $\delta^{13}C$ values between −8.5 and −8.3 vPDB.

The Sariol outcrop

The Hospital fault in this outcrop has an E-W striking and dips about 60°S. Fault zone thickness is about 1 m thick, and both footwall and hanging-wall of the Hospital fault have been deformed, unlike the previous outcrops (Fig. 8A,B). The Triassic dolostone constituting the hanging-wall next to the fault zone has been completely calcitized. It shows orange luminescence and has $\delta^{18}O$ values between −9.5 and −9.3 vPDB and $\delta^{13}C$ values between −4.8 and −4.7 vPDB. The first fracture generation identified in this outcrop is type-2 reverse faults (Fig. 8B). These faults generate a random breccia made of angulous granodiorite fragments cemented by two generations of calcite: C2b and C2c (Fig. 8C). Both generations are constituted by twinned calcite crystals up to 500 μm, being C2b brighter orange luminescent than C2c (Fig. 8D). C2b has higher contents of Mn and Fe, 3366 and 633 ppm on average, respectively, than C2c that has Mn values of 459 ppm in average and Fe contents below the detection limit. The high crosscutting relationship between both cements made impossible to pick them separately for isotopic analyses. The average values from both are of −5.8 vPDB for $\delta^{18}O$ and −7.2 vPDB for $\delta^{13}C$. The second generation identified is type-3D normal faults, which produced

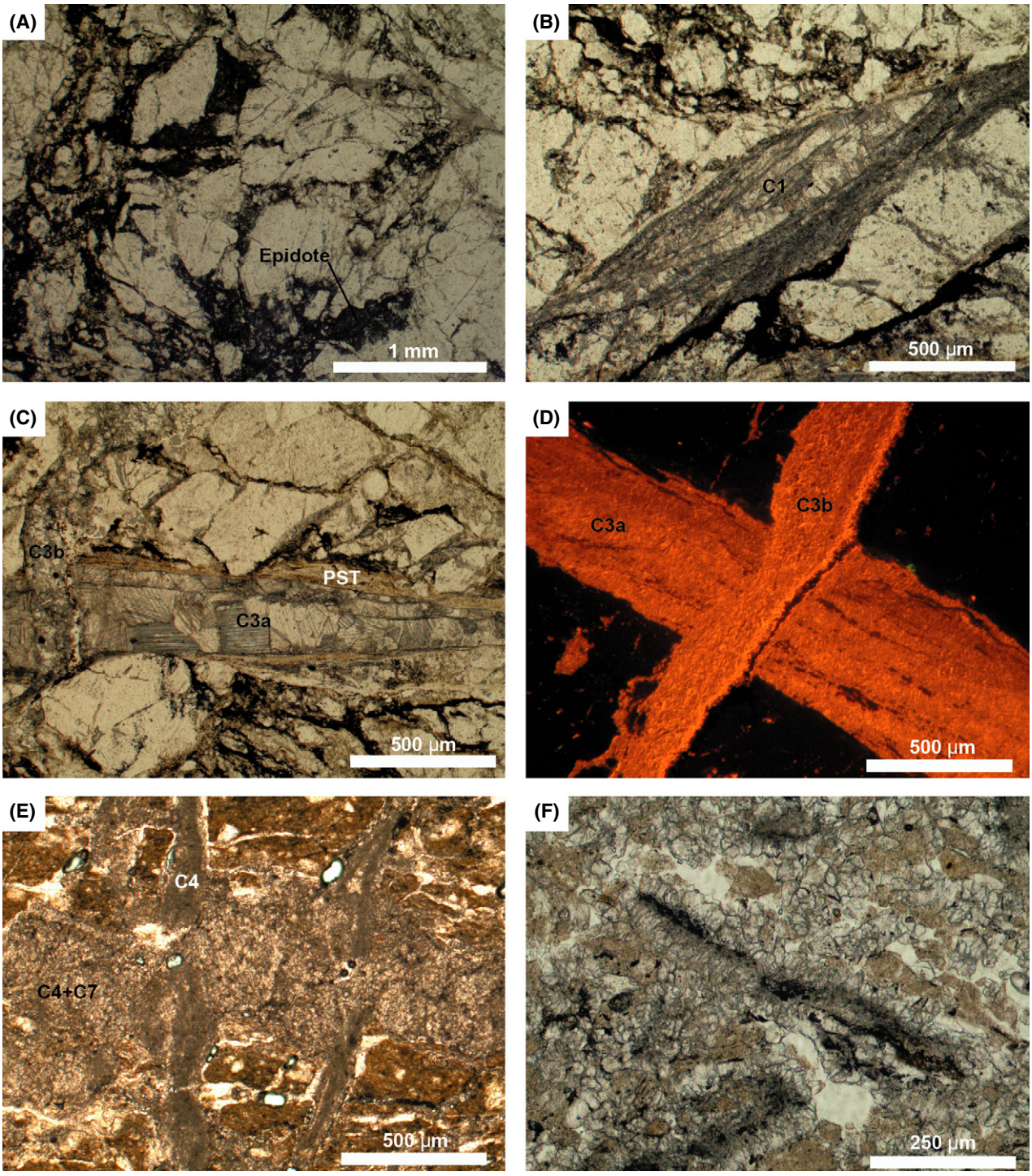

Fig. 7. Microphotographs of the minerals cementing the Hospital fault rocks in the Enric outcrop. (A) Random breccia cemented by epidotes (plane polarized light). (B) Multiepisodic pull-apart cemented by calcite C1 (plane polarized light). (C) Type-3A microfault formed by pseudotachylyte (PST) and later calcite cement C3a, which is crosscut by a type-3B open joint cemented by calcite C3b (plane polarized light). (D) Cathodoluminescence image of cements C3a and C3b. (E) Semicohesive breccia with fractures cemented by calcite C4. Calcite cement C7 partially replaces calcite C4 during soil development (plane polarized light). (F) Corn-cob aggregate formed by calcite C7 interpreted as a soil developed in the semicohesive gouge (plane polarized light).

cataclasites in the previous breccia and in the calcitized dolostone (Fig. 8B). In the former, subangulous clasts, from 10 µm to 2 mm in size, are contained in a fine grained matrix. In this matrix, parallel planes to the fracture border are cemented by a nonluminescent calcite-to-dolomite cement C5 (Fig. 8E). The cataclasite in the calci-

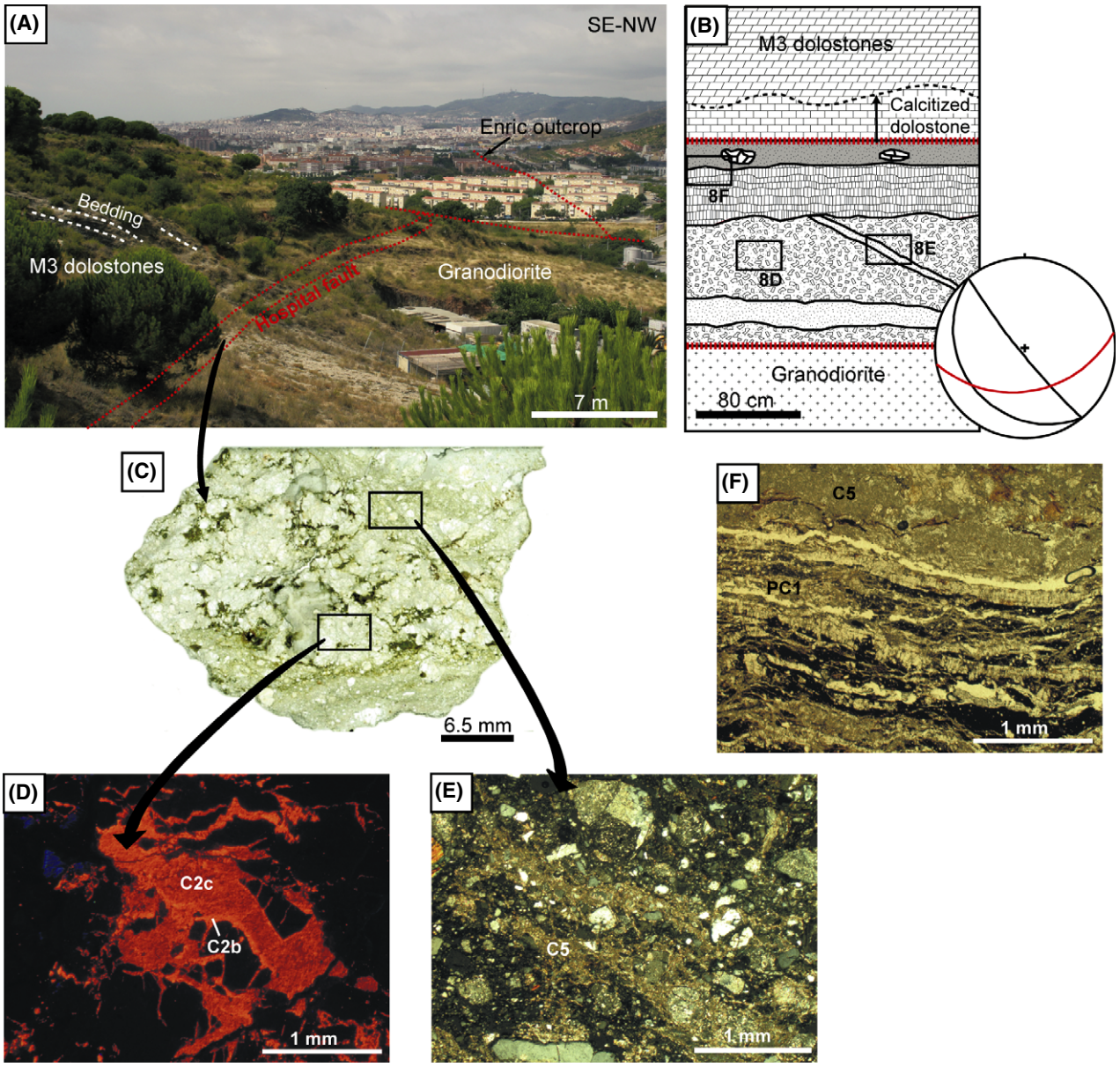

Fig. 8. Sariol outcrop. (A) View of the Hospital fault from the Sariol outcrop to the south-west. (B) Synthetic sketch of the fault zone at the Sariol outcrop and stereoplot of the sets of fractures. Red faults are type-2 faults reactivated during the development of type-3D faults (in black). (C) Thin section of fault rocks developed within the granodiorite. (D) Random breccia cemented by the two generations of calcite cement C2b and C2c (cathodoluminescence image). (E) Cataclasite developed in the granodiorite cemented by nonluminescent calcite-dolomite cement C5 (cross-polarized light). (F) Cataclasite in the calcitized dolostone cemented by calcite-dolomite cement C5 and succession of palisades PC1 (plane polarized light).

tized dolostone has a heterogeneous distribution of subrounded clasts from 200 μm to 5 mm in size, cemented by cement C5 (Fig. 8F). Fe values range from 576 to 8698 ppm. $\delta^{18}O$ values range from −2.9 to −2.6 vPDB, whereas the $\delta^{13}C$ is about −7.6 vPDB. Finally, the Hospital fault was cemented by palisade cement PC1. This cement displays a laminar disposition parallel to the main fault, and it is formed by submillimetric thick laminae (Fig. 8F). The palisade is formed by bladed crystals of low magnesium calcite, high magnesium calcite, and dolomite 200 μm long and 10 μm wide. The first laminae are constituted by nonluminescent dolomite, and high-Mg calcite (PC1a) and the last laminae are orange luminescent and are constituted by low-Mg calcite (PC1b). Vug porosity is cemented by the first cement (PC1a) in the calcitized dolostone cataclasite and by the second cement (PC1b) in the granodiorite cataclasite. PC1b has higher Mn and Fe contents than PC1a (Table 1). The palisade cement has $\delta^{18}O$ values between −2.7 and −1.9 vPDB and $\delta^{13}C$ values around −7.8 vPDB.

The Hospital fault hanging-wall

The horst is formed by Miocene rocks in the south and mostly Triassic rocks in the north (Fig. 2). As shown in Fig. 2, the boreholes reveal a major thickness of Miocene rocks in the south-west than in the north-east of the studied area and the lack of Triassic rocks in the south-east. In this domain, we have focused the study on the diagenesis of the Triassic dolostones and the evolution of deformation and fracture-related cements affecting these host rocks.

Deformation of the Miocene conglomerates and interpretation of the diagenetic processes sealing the faults in these conglomerates have been already published (Cantarero *et al.* 2010). The Miocene conglomerates are affected by minor type-3D normal faults constituted by a poorly developed fault core (up to 7 cm width) without a damage zone (Fig. 9A). Fault rocks are made of a red muddy material that has been obliterated by later diagenetic processes. The most important products are spherulites and palisades formed by orange bladed calcite. These crystals are nonluminescent although some of the spherulite nucleus are orange luminescent. Calcite ranges from low-to-high-Mg calcite. The $\delta^{18}O$ ranges from −4.4 to −3.9 vPDB, whereas the $\delta^{13}C$ has highly negative values that range from −10.3 to −9.0 vPDB. Luminescent orange bladed calcite has the less negative values, around −9.0 vPDB. These products result from pedogenic processes similar to Microcodium. The precipitation of the calcite crystals was induced by the evaporation from meteoric water together with biota activity although a neomorphism process from high-Mg calcite to low-Mg calcite was also taken into account. The presence of these pedogenic products has an important effect in fault evolution because (i) they date fault evolution during the Miocene extension; (ii) the presence of microfractures affecting the pedogenic products indicates a shallow burial depth and meteoric diagenetic environment during fault evolution; and (iii) they give the cohesiveness to the fault rock causing the sealing of the fault and its behavior as a barrier to fluids.

Within the Triassic rocks, different generations of fractures corresponding to three tectonic events have been identified. During the first tectonic event, type-1A faults generated cataclasites cemented by bright orange luminescent dolmicrite crystals D1 (Figs 9B,C and 10A,B). D1 has $\delta^{18}O$ values between −5.9 and −5.4 vPDB and $\delta^{13}C$ values between +2.3 and +2.4 vPDB. Later frictional processes produced ultracataclasites cemented by a red luminescent dolmicrite D2 with $\delta^{18}O$ values between −7.2 and −6.8 vPDB and $\delta^{13}C$ values between +2.5 and +2.6 vPDB (Fig. 10B). Dolomite D2 has different Fe content depending on the host rock. When precipitated in HR2 (D2a), it has Fe contents up to 870 ppm and an average of 440 ppm, whereas when precipitated in HR3 (D2b), it has contents up to 7803 ppm and an average of 2813 ppm. Finally, dolomite cement D3 precipitated within micrometric type-1A fractures. D3 is formed by anhedral crystals of dolomite, about 35 μm in size, which shows a zoned orange and red luminescence and grows in optic continuity with the host rock (Fig. 10B,C).

Minor type-2 reverse faults, which are the reactivation of the previous type-1A faults, have been also identified (Fig. 9D). Four generations of calcitized dolomite (from CD1 to CD4) have been associated with these faults. CD1 –CD4 cements are constituted by anhedral to subhedral crystals between 170 and 250 μm in size, with some idiomorphic rombohedral crystals pseudomorphs of the previous dolomite. These cements differ from each other in their luminescence behavior (Fig. 10C–E). CD1 shows an orange bright-zoned luminescence, CD2 shows a concentric zonation in orange and black, CD3 is nonluminescent with a bright orange luminescent thin line and CD4 is nonluminescent. These cements have Na, Mn and Fe contents below the detection limit and high contents of Sr, from 700 to 2200 ppm. It was difficult to sample these cements separately for isotopic analysis, and only cement CD3 could be sampled alone. However, the plot of all the values in a well-constrained area validates the use of all the data. The $\delta^{18}O$ values range between −5.9 and −4.9 vPDB, with an average about −5.3 vPDB, whereas the $\delta^{13}C$ values range between −7.4 and −5.4 vPDB, with an average about −6.3 vPDB.

Calcitization of the host dolostone has been locally observed in small patches. Under cathodoluminescence, the calcitized dolostone shows a bright orange thin line similar to cement CD3 (Fig. 10F). The $\delta^{18}O$ and $\delta^{13}C$ values are between the host rock and the calcite cements signatures, −4.1 vPDB and −3.2 vPDB, respectively.

During the third tectonic event, type-3A and type-3D normal faults and type-3E open joints were formed (Fig. 9E,F). Type-3A normal faults have a much localized deformation and generate slickensides.

After tectonic deformation, a karstic system was installed producing collapsed breccias and precipitating speleothems on the fault planes of fractures 3A and 3E (Fig. 9G,H). Speleothems are made of calcite, aragonite, high-Mg calcite, and dolomite and are formed by bladed and fibrous palisades, rafts or cavern pearls. These speleothems have high Sr contents, especially the ones formed by high-Mg calcite and aragonite, which can reach 7506 ppm in average and up to 13 800 ppm (Table 1). HMC speleothems with bladed morphology have $\delta^{18}O$ values between −5.3 and −4.7 vPDB and $\delta^{13}C$ values between −9.8 and −8.5 vPDB, whereas the HMC rafts have more enriched values, between −4.6 and −3.3 vPDB of $\delta^{18}O$ and between −9.0 and −8.2 vPDB of $\delta^{13}C$. The dolomite speleothems have the most $\delta^{18}O$-enriched values about −2.6 vPDB and $\delta^{13}C$ values about −9.3 vPDB. Finally, the aragonite spele-

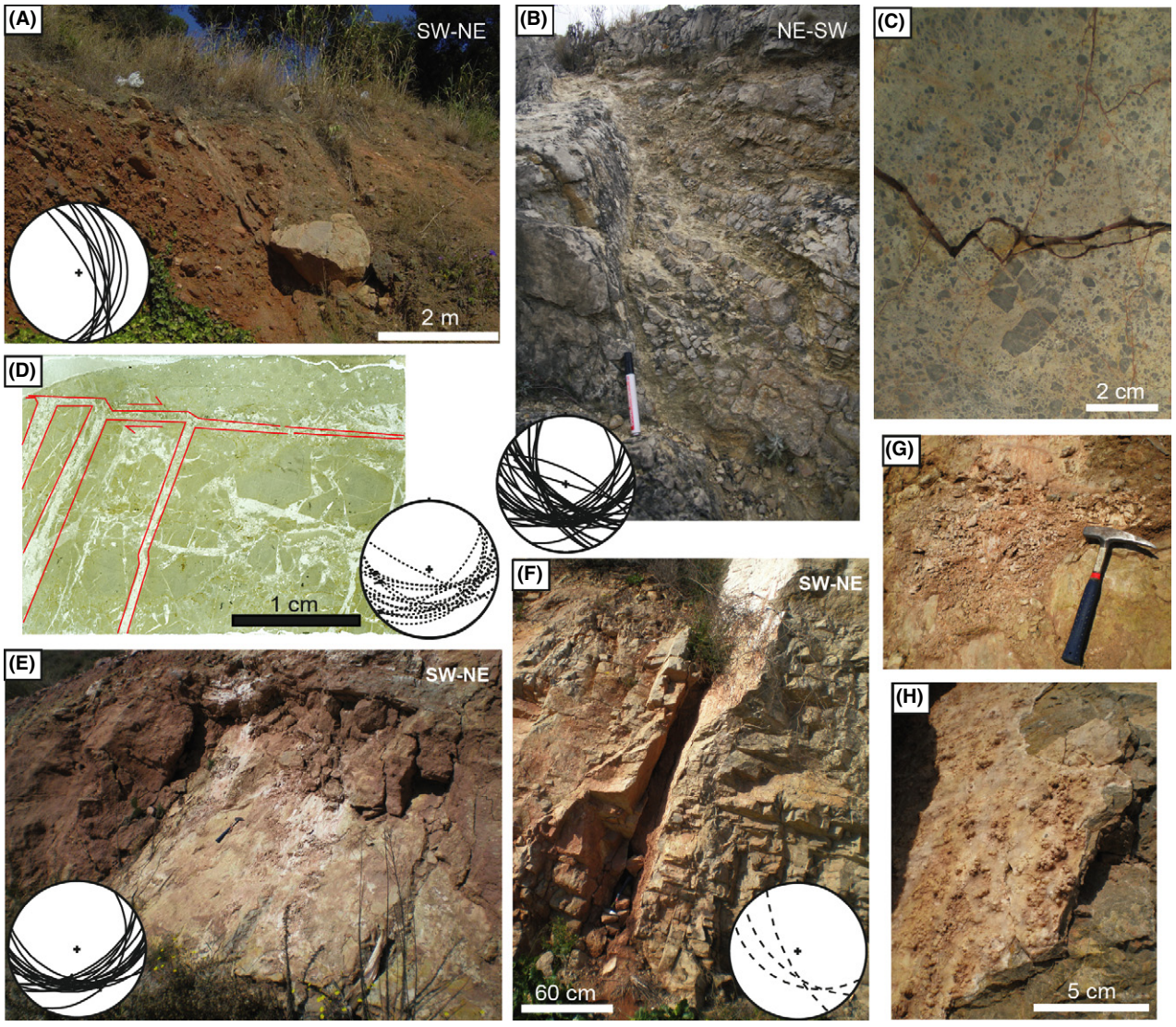

Fig. 9. Fractures of the hanging-wall. (A) Type-3D faults affecting the Miocene conglomerates. (B) Type-1A normal fault affecting carbonates of the M3 facies. (C) Cataclasite formed in the footwall of type-1A faults. (D) Microfault of type-2 within M1 facies. (E) Type-3A normal fault in M1 facies characterized by its undulating plane. (F) Type-3E open joint in M1 facies filled by clays of the M2. (G) Karstic breccias on a fault plane. (H) Speleothem covering one of the walls of a type-3E joint.

othems show $\delta^{18}O$ values between −4.6 and −4.2 vPDB and $\delta^{13}C$ values between −9.8 and −9.2 vPDB.

DISCUSSION

Evolution of fluids and relationships with tectonic events

The crosscutting relationships of fractures and the description of their fault rocks and cements presented in this paper, together with the knowledge of the sedimentology (Ramon & Calvet 1987; Calvet *et al.* 1990), diagenesis (Parcerisa 2002), petrology, and geochemistry of veins (Cardellach *et al.* 2002; Solé *et al.* 2002; Baqués *et al.* 2012), and structural works (Bartrina *et al.* 1992; Roca *et al.* 1999) of the Vallès-Penedès basin have allowed reconstructing the timing and characteristics of the paleofluids linked to fracturing in the studied area.

Mesozoic extension

Deposition of the Muschelkalk facies occurred in carbonate ramps during the Anisian (M1) and Ladinian (M3) (Calvet *et al.* 1990), synchronously to the first Mesozoic rifting event that lasted from Late Permian to Middle Jurassic (Salas & Casas 1993; Salas *et al.* 2001). Previous studies interpreted the dolomitization of M1 facies penecontemporaneous to sedimentation (Virgili 1957). On the other hand, Ramon & Calvet (1987) suggested that the upper dolomitic units were of primary origin, but the lower ones were the

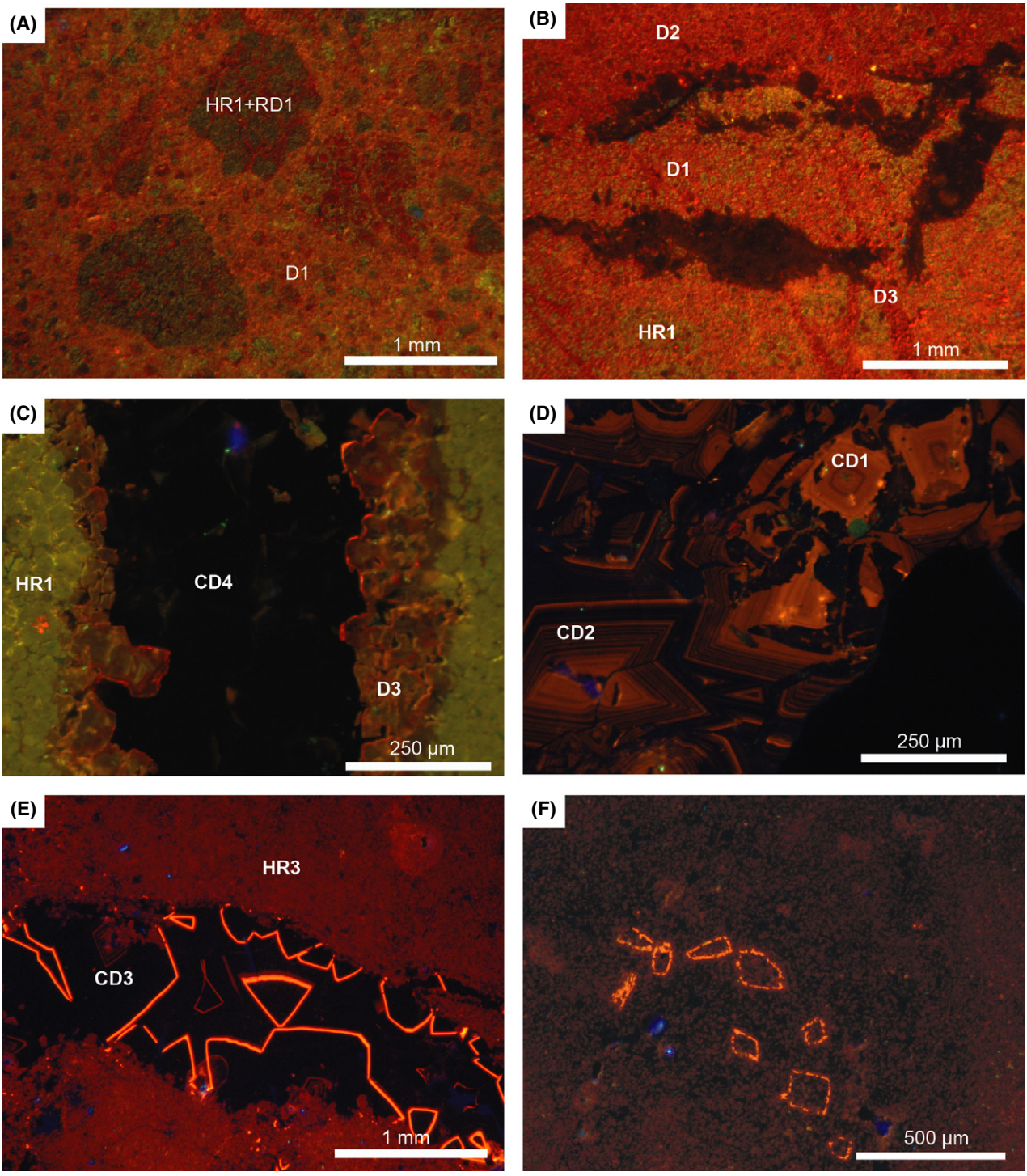

Fig. 10. Microphotographs of the minerals cementing minor fractures within Triassic dolostones of the Hospital hanging-wall. (A) Cataclasite cemented by dolomite cement D1 developed in type-1A faults. Observe the red dull replacive dolomite within the clasts (cathodoluminescence). (B) Cataclasite and later ultracataclasite cemented by dolomite cements D1 and D2, respectively. Also, later fractures cemented by dolomite cement D3 are observed (cathodoluminescence). (C) Dolomite cement D3 and later calcitized dolomite CD4 (cathodoluminescence). (D) Cathodoluminescence image of calcitized dolomite cements CD1 and CD2. (E) Cathodoluminescence image of calcitized dolomite cement CD3. (F) Patch of calcitized dolostone with the same cathodoluminescence behavior than the CD3 cement.

result of a *mixed water* model of dolomitization. With regard to M3 facies, Tucker & Marshall (2004) proposed an early dolomitization from seawater and a later recrystallization as the responsible of the $\delta^{18}O$-shift toward more depleted values. The $\delta^{18}O$ and $\delta^{13}C$ values of the M1 and M3 dolostones cropping out in the studied area fall within the box of the Anisian-Ladinian seawater (Veizer *et al.* 1999) (Fig. 11). Moreover, HR1 and HR3 show nondestructive fabrics, indicating that dolomitization occurred during an early event (Tucker & Marshall 2004). Both points suggest that dolomitization was produced by marine Triassic waters almost coevally to sedimentation. However, M1 facies suffered two dolomitization processes as denoted by the presence of the replacive dolomite RD1, which is probably related with the dolomitization of M3 facies.

Also, the first dolomite cement D1 associated with fractures type-1A fall within the seawater values, indicating the onset of the Triassic rifting under marine conditions (Fig. 11). Dolomite cement D2, and probably also D3, associated with fractures type-1A, shows more $\delta^{18}O$-depleted values but the same $\delta^{13}C$ values than the host rocks and cement D1. Moreover, the elemental geochemistry of dolomite cement D2 is controlled by the host rock in which is precipitating, suggesting a high fluid–rock interaction. These facts point to the crystallization of dolomite cements from the marine water during increasing burial, produced by the rifting, in a closed hydrological regime.

The cements attributed strictly to the Hospital fault during the Mesozoic are quartz and later calcites C1 and chlorites in type-1B faults. This association of quartz and later calcite has been also described in the Montnegre Horst associated with the second Mesozoic rifting event (Late Jurassic–Late Cretaceous) (Cardellach *et al.* 2002). Calcites C1 show $\delta^{18}O$-depleted values (Fig. 11) that combined with fluid inclusion data in quartz and calcites (Cardellach *et al.* 2002) points to hydrothermal fluids (180–230°C). The solubility/precipitation of vein minerals is dependent on fluid temperature, pressure, and composition (Parry 1998). Taking into account that these rocks have not been

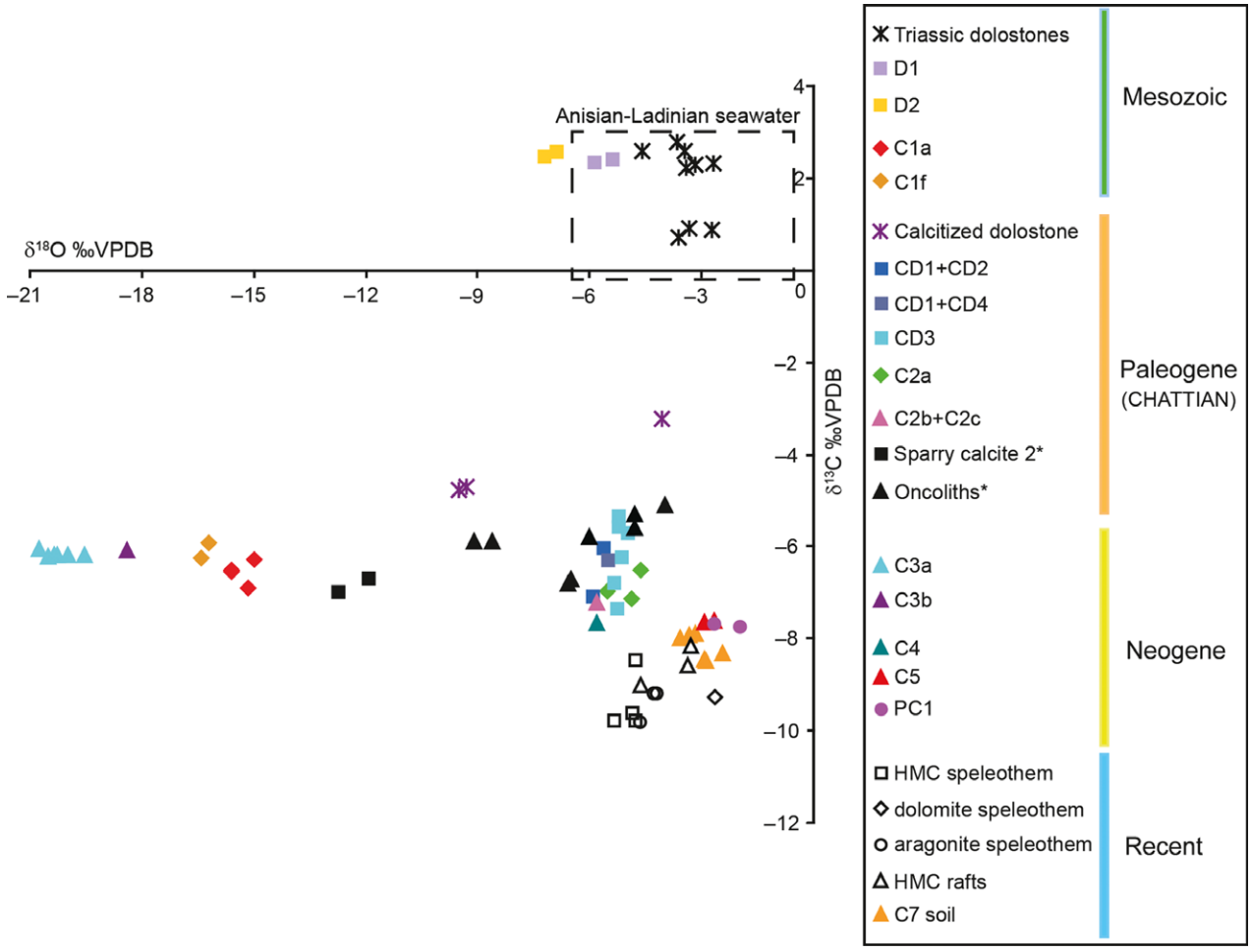

Fig. 11. $\delta^{18}O$ versus $\delta^{13}C$ plot of the different carbonate cements and host rocks. The asterisk marks the values of the calcites of Parcerisa (2002). Anisian-Ladinian seawater values are according to Veizer *et al.* (1999).

subjected to important changes in pressure (Juez-Larré 2003), temperature, and composition are the most important factors in our context. The equations of Clayton *et al.* (1972) and O'Neil *et al.* (1969) were applied in quartz and calcite, respectively, to establish the parental fluid of the hydrothermal brine. The first equation gives values of $\delta^{18}O_{water}$ between −1.2 and +3.2 SMOW, indicating that the brine had a marine origin, as it was already postulated by Cardellach *et al.* (2002). However, the equation of O'Neil *et al.* (1969) indicates that calcite C1 precipitated from water with $\delta^{18}O$ values between +7 and +10 SMOW. Most granitic rocks have $\delta^{18}O$ values between +7 and +13 SMOW and δD values between −85 and −50 SMOW (Taylor 1977). Isotopic studies of the late Hercynian intrusive rocks of the Montnegre Horst (CCR) show $\delta^{18}O$ values up to +6.1 SMOW and δD values up to −35 SMOW, suggesting the hydrothermal alteration of the rock by a $\delta^{18}O$-depleted fluid with a low water/rock ratio (Solé *et al.* 2002). The $\delta^{18}O$-depleted fluid could have got different origins as its signal has been completely buffered by the granitic host rock.

Paleogene compression

Type-2 reverse faults and their related cements C2a to C2c and CD1 to CD4 are attributed to this period. These cements show $\delta^{18}O$ and $\delta^{13}C$ values ranging from −5.9 to −4.6 VPDB and −7.4 to −5.4 VPDB, respectively, coinciding with the values of the calcites defined by Parcerisa (2002), affecting the Oligocene rocks of the horst (Fig. 11), which were attributed to the last compressional stage that occurred during the Chattian. The isotopic signal indicates their meteoric origin. The $\delta^{18}O$ and $\delta^{13}C$ values of the calcitized dolostone, from −9.5 to −4.1 VPDB and from −4.8 to −3.2 VPDB, respectively, fall between those of the Triassic dolostones ($\delta^{18}O$ between −4.6 and −2.7 VPDB and $\delta^{13}C$ between +0.7 and +2.8 VPDB) and those of the cements attributed to this period. In conclusion, the Paleogene compression is characterized by the opening of the hydrological system, which allows the percolation of meteoric fluids responsible of the calcite cements and the calcitization of the dolomite, which is favoured by the uplift of the horst. This conclusion is in agreement with the results of the work of Baqués *et al.* (2012) about the south-western end of the Penedès fault affecting Cretaceous rocks.

Neogene extension

Type-3 fractures have been associated with the Neogene extension because of the implied host rocks, their extensional character, and the crosscutting relationships with previous fractures. Type-3A normal faults and type-3B joints have been related to the syn-rift stage produced during the Aquitanian?- late Burdigalian. The development of pseudotachylytes in type-3A faults indicates the seismic activity of some fault segments at the onset of the Neogene extension at about 2.3 km depth (maximum depth conditions according to Juez-Larré (2003)). Later calcites associated with these fractures (C3a and C3b, respectively) show $\delta^{18}O$-depleted values (Fig. 11) similar to the ones reported by Cardellach *et al.* (2002) and Travé & Calvet (2001), both attributing these values to the Neogene syn-rift. Temperatures of these calcites obtained from fluid inclusion data by Cardellach *et al.* (2002) range between 130 and 150°C. Taking into account these temperatures, a surface paleotemperature of 20°C, and the depth conditions during the syn-rift, the calculated geothermal gradient ranges between 47 and 56°C/km, higher than the estimated geothermal gradient during the Neogene (30°C/km according to Juez-Larré (2003)), indicating the hydrothermal character of the fluids. With regard to their origin, applying the equation of O'Neil *et al.* (1969), results of $\delta^{18}O$ of the waters between −0.9 and +1.5 SMOW are obtained what would imply a seawater source. Although sedimentation from Chattian to late Miocene has been dominated by alluvial fans, during the late Burdigalian shore environments existed in the area (Parcerisa 2002; Riba & Colombo 2009 and references therein). Thus, waters responsible of the precipitation of calcites C3a and C3b during the syn-rift were topographically driven meteoric waters, warmed at depth and buffered by the host granodiorites, and mixed with marine waters during their upflow. Moreover, these waters were partially yielding to such a positive values. This significant water–rock interaction is also recorded by the low $\delta^{13}C$ values of these calcites, which are probably due to the influence of organic matter. The most probable source for the low $\delta^{13}C$ is the Silurian black shales that crop out in the area, with TOC content between 3% and 8.6%. The same phenomenon is recorded in the Mesozoic calcites.

Type-3C seams have been related to a small compression event that took place during the early postrift (late Langhian to Serravalian) by comparison with similar type and orientation of fractures in the neighbor Penedès graben (Baqués *et al.* 2012).

Finally, type-3D normal faults, type-3E open joints, and later speleothem and soil development formed during the late postrift (Serravalian to recent). Their related low-Mg calcite, high-Mg calcite, dolomite, and aragonite cements are characterized by an important increase in the Mg content (from calcite to dolomite), and they are significantly more enriched in the $\delta^{18}O$ content and depleted in the $\delta^{13}C$ content than the previous cements (Fig. 11). Therefore, these geochemical characteristics indicate again the opening of the system and the percolation of meteoric waters with a strong influence of soil-derived CO_2. In consequence, during this last stage of the Neogene extension, fault activity occurred under subaerial conditions. Also, the palisade cement PC1 with morphology and mineralogy

indicating their formation in the vadose zone, with fluctuating water conditions, supports this hypothesis. With regard to the $\delta^{18}O$ values, they are slightly enriched with respect to the common meteoric waters. Microcodium formed in minor faults affecting the Miocene conglomerates occurred during the beginning of the late postrift in a temperate climate, explaining the enriched $\delta^{18}O$ values by an evaporation effect (Cantarero *et al.* 2010). Calcite cement C5 and palisade cement PC1, probably related to the sigmoidal microfractures affecting the Microcodium, formed in the same context. On the opposite, speleothems affecting the Triassic dolostones and the soil developed within the Hospital fault in the Enric outcrop formed later, after the cessation of fault activity. Similar isotopic compositions to these features have also been described in Pleistocene speleothems in the south of the Iberian Peninsula and in the Mallorca Island (Vesica *et al.* 2000; Jiménez de Cisneros *et al.* 2003) and Tertiary speleothems developed in the Ramales Platform (Basque–Cantabrian Basin) (Dewit *et al.* 2012), suggesting a widespread event in the Iberian Peninsula from the Tortonian to recent. These values have been interpreted as originated from meteoric waters in a colder period than present (Vesica *et al.* 2000; Jiménez de Cisneros *et al.* 2003).

The Hospital fault growth and fluid flow paths

Fault rocks show differences on neoformed minerals between the outcrops studied in the Hospital fault. These mineralogical differences along the fault mark preferential paths for fluids in certain periods of time, probably related to the independent tectonic activity of fault segments or different fluid origin through time related to intermittent pulses of fluids.

The independent origin and tectonic activity of the fault segments is supported by the differences in strike and dip between the fault segments but also by the thickness of the Triassic rocks and distribution of the cements. There is a strong difference in the thickness of the Triassic rocks along the horst. In the south, they are almost absent, whereas in the north they have a thickness up to 200 m (Fig. 12A). In the CCR, the changes in thickness within the Triassic rocks have been related to the influence of NE-SW and NW-SE normal faults (Calvet *et al.* 1990). So probably, in the studied sector of the Barcelona Plain, during the Triassic extension, the Hospital fault was formed by two fault segments that controlled the sedimentation. The southern segment, where the Hospital outcrop is settled, is a low-angle normal fault (<30°SE), whereas the northern segment (Sariol outcrop location) has a dip around 55°SE. This difference in dip control the vertical throw of the fault and could lead to a thicker accommodation space in the northern segment. The southern segment has low dip probably because: (i) it is the deep section of a listric Mesozoic fault, or (ii) it is the rework as a normal fault of the Permian unconformity between the granodiorite and the Triassic rocks that crops out along the CCR.

Cements associated with the Cretaceous rifting are only identified in the Hospital and Enric outcrops (southern segment), indicating a localized migration of hot fluids ascending through the fault during its displacement (Fig. 12B). The lack of these cements in the north could be due to the inactivity of this segment or the erosion of the cements associated with this period. After these rifting events, the Paleogene compression inverted the previous normal faults and produced the exhumation and folding of the Triassic units. In the southern segment, the erosion of the Triassic rocks was almost complete as it is shown by the boreholes. The uplift of the Triassic rocks in the north favoured the percolation of meteoric fluids and the calcitization of the dolostones and dolomite cements (Fig. 12C).

The thickness of the Miocene rocks decreases toward the north-east (Fig. 2) due to the differential displacement of the fault segment, indicating the presence of the fault tip in the area of the Enric outcrop. The fault rocks and cements attributed to the Neogene syn-rift (PST and calcite C3a and C3b) have only been identified in the Enric outcrop. This fact has been interpreted as the result of fault growth by tip propagation of the southern segment (Figs 12D and 13). Tip propagation produces the migration of the process zone to the north, which is formed by arrays of fractures constituted by fracture sets parallel to the southern segment and to the new fault trace that is forming between the two segments (Fig. 13). Each slip event of the main fault involves the propagation and linkage of the previous arrays generating 3A microfaults. These linking structures have been demonstrated to develop friction melts (Swanson 1992), which would explain the formation of pseudotachylytes in type-3A faults in this point. Studies in seismically active fault systems have also shown the spatial relationship between seismicity and linking structures between main faults (Tavarnelli & Pasqui 2000). Following crack-seals cemented by calcite C3a could be generated during the preseismic stage of a new earthquake (Sibson 1986). Deformation under an extensional stress regime generates structures in the process zone that enhance dilation and therefore permeability, generating zones of localized hydrothermal upflow (Rowland & Sibson 2004). Moreover, outflows of water following earthquakes are not an infrequent phenomenon (seismic pumping (Sibson *et al.* 1975)), which enter and cement accessible extension fractures such as 3B joints.

During the late postrift, both segments had some displacement (Fig. 12E). This displacement was produced at shallow conditions in the presence of low-temperature meteoric fluids. Finally, NW-SE strike-slip faults segmented again the fault generating the current disposition probably during the Messinian compression (Fig. 12F). Large-scale

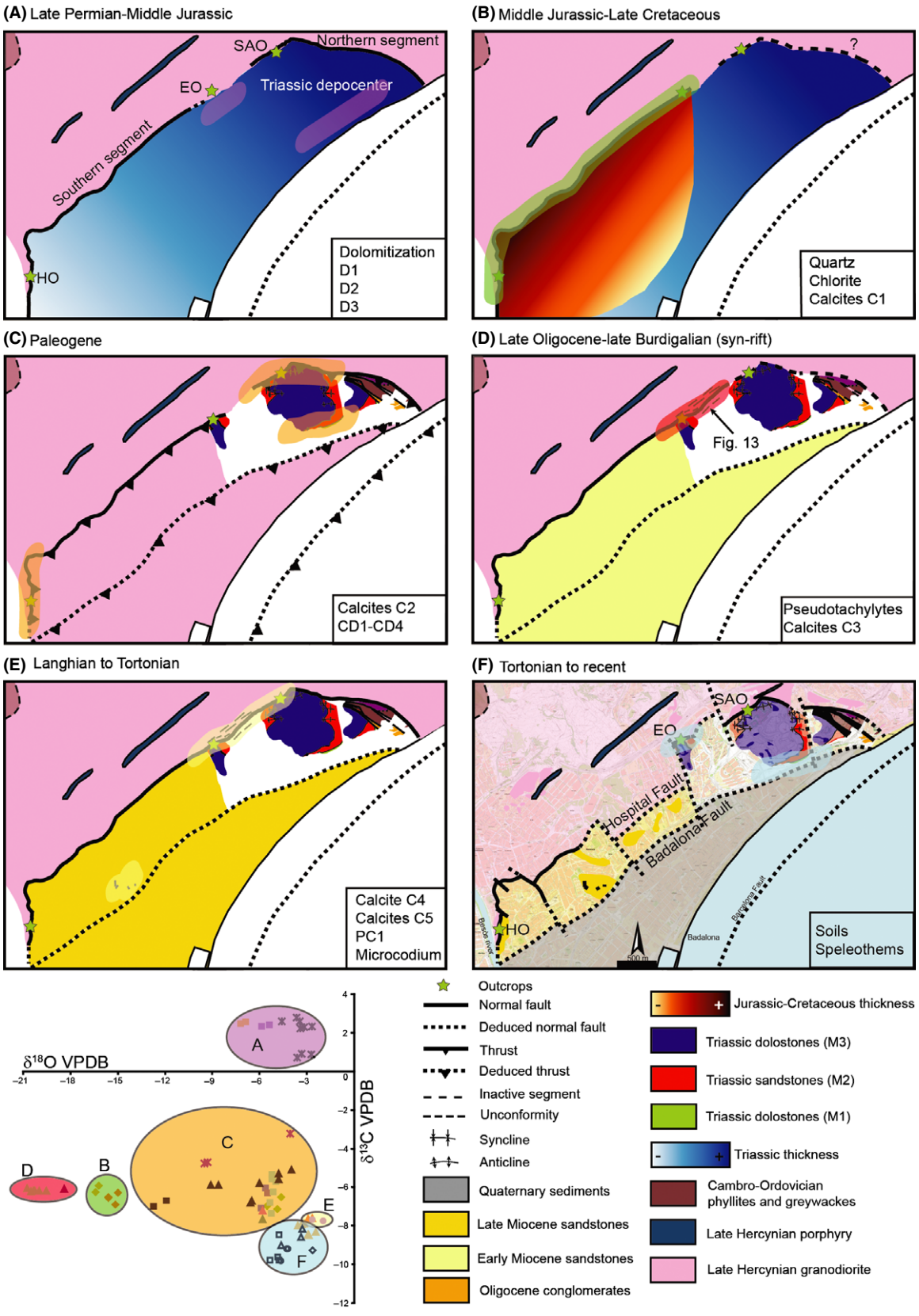
(A) Late Permian-Middle Jurassic
SAO
Northern segment
EO
Triassic depocenter
Southern segment
HO
Dolomitization
D1
D2
D3
(B) Middle Jurassic-Late Cretaceous
?
Quartz
Chlorite
Calcites C1
(C) Paleogene
Calcites C2
CD1-CD4
(D) Late Oligocene-late Burdigalian (syn-rift)
Fig. 13
Pseudotachylytes
Calcites C3
(E) Langhian to Tortonian
Calcite C4
Calcites C5
PC1
Microcodium
(F) Tortonian to recent
SAO
EO
Hospital Fault
Badalona Fault
HO
Soils
Speleothems
δ18O VPDB
δ13C VPDB
A
B
C
D
E
F
Outcrops
Normal fault
Deduced normal fault
Thrust
Deduced thrust
Inactive segment
Unconformity
Syncline
Anticline
Quaternary sediments
Late Miocene sandstones
Early Miocene sandstones
Oligocene conglomerates
Jurassic-Cretaceous thickness
Triassic dolostones (M3)
Triassic sandstones (M2)
Triassic dolostones (M1)
Triassic thickness
Cambro-Ordovician phyllites and greywackes
Late Hercynian porphyry
Late Hercynian granodiorite

Fig. 12. Structural evolution of the basin and distribution and evolution of fluids through time in the northern sector of the Barcelona Plain from Late Permian to Recent. (A) Deposition of the Triassic rocks and dolomitization during the first Mesozoic rifting event. (B) Cretaceous rifting localized in the southern segment and circulation of ascending hot fluids. (C) Basin inversion, folding, erosion, and percolation of low-temperature meteoric fluids that produce the calcitization of previous dolomites. (D) Segment connection through fault growth and upflow of hot fluids in the relay area during the Neogene syn-rift. (E) Propagation of the Hospital fault to the surface and percolation of low-temperature meteoric fluids. (F) Generation of the NW-SE set of fractures that segment the Hospital fault and development of soil and speleothems.

horizontal fluid flow is prevented by the marked structural heterogeneities produced by the variations of fault zone architecture along strike.

Origin of the hydrothermalism

The onshore of the CCR is characterized by the presence of hot water springs, up to 70°C, mainly along the main bounding faults. And, although Miocene crustal thinning and Miocene and Quaternary volcanism have been reported in the area, this region of the Iberian Peninsula cannot be defined as a high-temperature geothermal province (Fernández & Banda 1989). All the studies support the origin of these springs as meteoric waters infiltrated through fractured elevated areas (horsts) that have been warmed at greater depths by a normal geothermal gradient (Fernández & Banda 1989; Carmona *et al.* 2000). This mechanism of fluid flow has been also postulated at the onset of the Neogene in the Penedès half-graben (Bitzer *et al.* 2001), where meteoric waters would have been topografically driven, through the fault zones, thanks to the elevation of the shoulders and the subsidence of the basin during the extensional event. In the case of the Barcelona Plain, meteoric waters were mixed with seawater due to its position at the shoreline. In later stages due to erosion and the consequent lose of topographical gradient, this mechanism stops, explaining the lack of hot waters during the postrift.

Crustal thinning and geothermal gradients during the Mesozoic and the Neogene extension were quite similar and therefore indicating crustal thinning was neither the reason for Mesozoic hydrothermalism (Roca 1996; Juez-Larré 2003). Mesozoic volcanism has been identified related to the first rifting in the southern CCR (150 km to the south of the Barcelona Plain) and in the Iberian Chain (Ortí & Vaquer 1980; Mitjavila & Martí 1986). This volcanism was produced by an extended volcanic complex in this area (Ortí & Vaquer 1980). Also, in the Iberian Chain, Albian-Coniacian volcanism, metamorphism and Hg-Sb deposits have been related to the emplacement of a hot spot in the offshore opposite to San Sebastian (northern Spain), which would produce the emplacement of a basic pluton below the Iberian Chain and the extrusion of alkali basalts in the Pyrenees (Aller & Zeyen 1996; Salas *et al.* 2005). However, in the central CCR, where this work is performed, there are no evidences of such magmatism. Moreover, fission-track data in this area perfectly link with structural and sedimentological

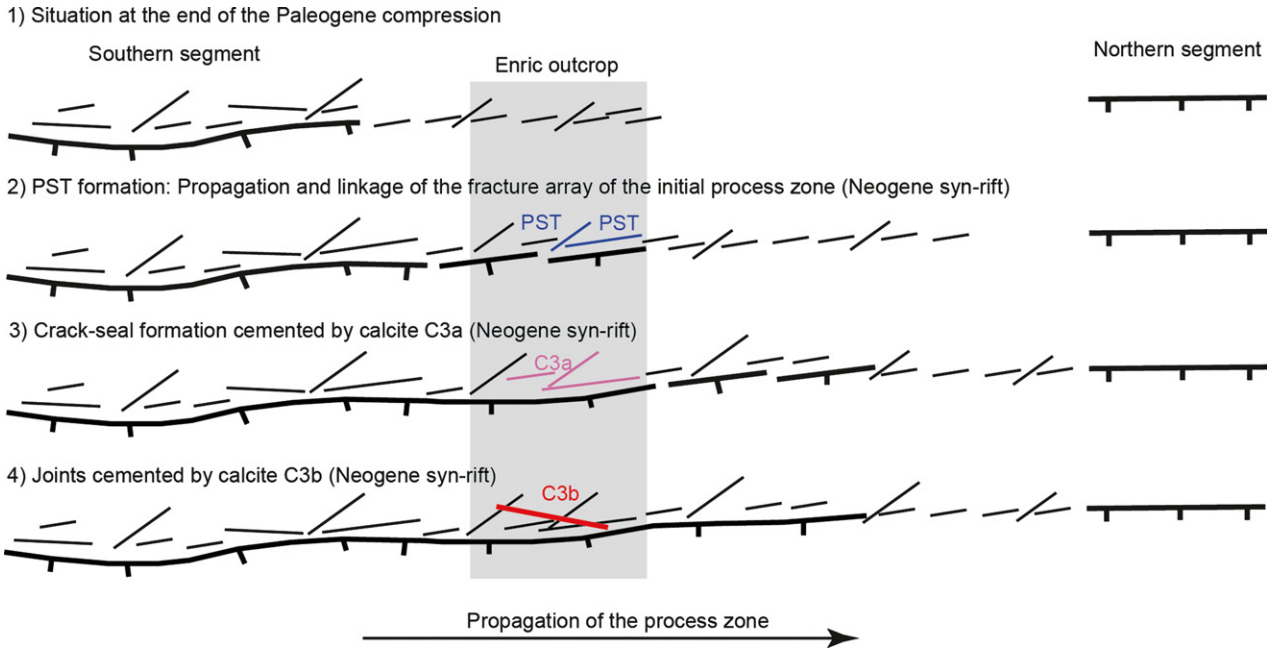

Fig. 13. Sketch of the mechanism of fault growth by tip propagation of the southern segment at kilometric scale. PST is the abbreviation of pseudotachylyte.

observations and only in specific points, generally next to fault zones, fission-track data are reset (Juez-Larré 2003). The second Mesozoic rifting mostly took place under marine conditions; however, prolonged periods of emersion occurred during Berriasian–Barremian times (Ebro Massif), probably controlled by normal faulting. This emersion is shown by the presence of karstification and bauxite formation in Kimmeridgian rocks outcropping close to the Barcelona Plain (Combes 1969; Molina & Salas 1993; Salas *et al.* 2004). As discussed in section 7.1, fluids responsible of calcite C1 precipitation during the second Mesozoic rifting were brines highly interacted with the host rock that could have got several origins. Taking into account the geomorphological configuration during this period, the most plausible mechanism for such hydrothermal fluids was the infiltration of meteoric waters through the emerged areas (topography driven) that have been warmed at depth and that during their upflow through the main fault mixed with marine waters expulsed from the sediments by compaction. This mixing between fluids could have been responsible for the oscillating cathodoluminescence behavior of cements C1.

CONCLUSIONS

The Hospital fault and its hanging-wall in the northern sector of the Barcelona Plain recorded three main tectonic events characterized by cements resulting from successive circulation of hydrothermal and low-temperature meteoric fluids. Hydrothermal fluids are characteristic of extensional events, whereas low-temperature meteoric fluids are found in both extensional and compressional events. A topographically driven fluid mechanism, favoured by the shoulder uplift produced during normal faulting, was responsible for the hydrothermal fluids.

During the Late Permian–Middle Jurassic rifting stage, the Hospital fault controlled the thickness and distribution of the Triassic sediments, having their depocenter to the north. Their early dolomitization produced by Triassic seawater took place at shallow conditions. Dolomite cements in type-1A fractures were produced by the Triassic seawater during increasing burial in a relatively closed hydrological regime. Fault activity during the second Mesozoic rifting stage (Late Jurassic-Late Cretaceous) was localized in the southern segment, and it is represented by type-1B faults. This stage is characterized by hydrothermal brines of meteoric origin, with temperatures over 180°C, which ascended through the southern fault segment and mixed with marine water, precipitating quartz, chlorite, and calcite C1.

The Paleogene compression in this area was late (Chattian) and it is marked by type-2 fractures. The compression produced exhumation, folding, and erosion of the Cretaceous and almost all the Triassic rocks in the south of the studied area. The uplift favoured the percolation of low-temperature meteoric fluids that produced the calcitization of the dolostones and of the dolomite cements.

During the Aquitanian-late Burdigalian syn-rift stage, the southern segment of the Hospital fault grew by propagation of its northern tip. Fault growth generated minor type-3A and type-3B fractures in the relay zone, which are characterized by the formation of pseudotachylytes and the later precipitation of calcite C3. This calcite is the result of the localized upflow of hydrothermal brines with temperature about 140°C, which are the result of warmed meteoric waters at depth mixed with marine waters during their upflow. Thus, the increase in dilatancy produced in the process zone together with a seismic pumping effect control the upflow during fault growth. Type-3C seams have been related to a small compressional stage within the early postrift. During the late postrift, the Hospital fault acted as a unique segment. Type-3D and type-3E fractures were formed at shallow conditions and under a low-temperature meteoric regime. Later, possibly during the Messinian, the NW-SE strike-slip faults were formed and offset the Hospital fault to its current configuration.

In conclusion, the tectonic regime, the fault zone architecture, and the seismic activity controlled the fluid regime and the fluid flow pathways in the Barcelona Plain from Mesozoic to recent.

ACKNOWLEDGEMENTS

We are grateful with Jordi Illa for sample preparations and with the Thin Section Service of the Universitat de Barcelona. The stable isotopy, the electron microprobe, and the SEM analyses were carried out at 'Serveis Científico-Tècnics' of the Universitat de Barcelona. We also thank Jordi Jubany from GISA, Estibalitz Allende from Payma and Geotec-262 for the information and core samples provided from the boreholes of the several ongoing civil engineering works in Barcelona. This research was performed within the framework of DGICYT Spanish Project CGL2010-18260, *Grup Consolidat de Recerca* 'Geologia Sedimentària' (2009SGR-1451) and the 2010FI_B2 00179 supported by the Comissionat per a Universitats i Recerca del Departament d'Innovació, Universitats i Empresa de la Generalitat de Catalunya i el Fons Social Europeu. The constructive comments of two anonymous referees helped to improve the quality of the manuscript.

REFERENCES

Albert JF, Corominas J, París C (1979) El estudio hidrogeológico de los manantiales y su aplicación geológica: caso de las aguas termales, carbónicas y sulfhídricas de Cataluña. *Acta Geologica Hispànica. Homenatge a Lluís Solé i Sabarís*, **14**, 391–4.

Aller J, Zeyen HJ (1996) A 2.5-D interpretation of the Basque country magnetic anomaly (northern Spain): geodynamical implications. *Geologische Rundschau*, **85**, 303–9.

Anadón P, Cabrera L, Guimerà J, Santanach P (1985) Paleogene strike-slip deformation and sedimentatiom along the southeastern margin of the Ebro Basin. In: *Strike-slip Deformation, Basin Formation Sedimentation* (eds Biddle KT, Christie-Blick N) *Special Publication of the Society of Economic Paleontologists and Mineralogists*, **37**, 303–18.

Andre G, Hibsch C, Fourcade S, Cathelineau M, Buschaert S (2010) Chronology of fracture sealing under a meteoric fluid environment: microtectonic and isotopic evidence of major Cainozoic events in the eastern Paris basin (France). *Tectonophysics*, **490**, 214–28.

Ashauer H, Teichmüller R (1935) Die variszische und alpidische Gebirgsboldung Kataloniens. Abhandlungen Gesellschaft Wissenschaften Göttingen, Math Phys. K1, 3F, 16.

Baqués V, Travé A, Benedicto A, Labaume P, Cantarero I (2010) Relationships between carbonate fault rocks and fluid flow regime during propagation of the Neogene extensional faults of the Penedès basin (Catalan Coastal Ranges, NE Spain). *Journal of Geochemical Exploration*, **106**, 24–33.

Baqués V, Travé A, Roca E, Marín M, Cantarero I (2012) Geofluid behaviour in successive extensional and compressional events: a case study from the southwestern end of the Vallès-Penedès Fault (Catalan Coastal Ranges, NE Spain). *Petroleum Geoscience*, **18**, 17–31.

Bartrina MT, Cabrera L, Jurado MJ, Guimerà J, Roca E (1992) Evolution of the central Catalan margin of the Valencia trough (western Mediterranean). *Tectonophysics*, **203**, 219–47.

Bastesen E, Braathen A, Nøttveit H, Gabrielsen RH, Skar T (2009) Extensional fault cores in micritic carbonate-case studies of the Gulf of Corinth, Greece. *Journal of Structural Geology*, **31**, 403–20.

Berg SS, Skar T (2005) Controls on damage zone asymmetry of a normal fault zone: outcrop analyses of a segment of the Moab fault, SE Utah. *Journal of Structural Geology*, **27**, 1803–22.

Billi A (2010) Microtectonics of low-P low-T carbonate fault rocks. *Journal of Structural Geology*, **32**, 1392–402.

Bitzer K, Travé A, Carmona JM (2001) Fluid flow processes at basin scale. *Acta Geologica Hispanica*, **36**, 1–20.

Boles JR, Eichhubl P, Garven G, Chen J (2005) Evolution of a hydrocarbon migration pathway along basin-bounding faults: evidence from fault cement. *AAPG Bulletin*, **88**, 947–70.

Breesch L, Swennen R, Vincent B (2009) Fluid flow reconstruction in hanging and footwall carbonates: compartmentalisation by Cenozoic reverse faulting in the Northern Oman Mountains (UAE). *Marine and Petroleum Geology*, **26**, 113–28.

Bussolotto M, Benedicto A, Invernizzi C, Micarelli L, Plagnes V, Deiana G (2007) Deformation features within an active normal fault zone in carbonate rocks: the Gubbio fault (Central Apennines, Italy). *Journal of Structural Geology*, **29**, 2017–37.

Caine JS, Evans JP, Forster CB (1996) Fault zone architecture and permeability structure. *Geology*, **24**, 1025–8.

Calvet F, Tucker ME, Henton JM (1990) Middle Triassic carbonate ramp systems in the Catalan Basin, northeast Spain: facies, systems tracts, sequences and controls. *Special Publications International Association of Sedimentologists*, **9**, 79–108.

Calvet F, Travé A, Roca E, Soler A, Labaume P (1996) Fracturación y migración de fluidos durante la evolución tectónica neógena en el Sector Central de las Cadenas Costero Catalanas. *Geogaceta*, **20**, 1715–8.

Canals À, Cardellach E (1997) Ore lead and sulphur isotope pattern from the low-temperature veins of the Catalonian Coastal Ranges (NE Spain). *Mineralium Deposita*, **32**, 243–9.

Cantarero I, Travé A, Alías G, Baqués V (2010) Pedogenic products sealing normal faults (Barcelona Plain, NE Spain). *Journal of Geochemical Exploration*, **106**, 44–52.

Cardellach E, Canals À, Grandia F (2002) Recurrent hydrothermal activity induced by successive extensional episodes: the case of the Berta F-(Pb-Zn) vein system (NE Spain). *Ore Geology Reviews*, **22**, 133–41.

Carmona JM, Bitzer K, López E, Bouazza M (2000) Isotopic composition and origin of geothermal waters at Caldetes (Maresme-Barcelona). *Journal of Geochemical Exploration*, **69–70**, 441–7.

Cherchi A, Montadert L (1982) Oligo-Miocene rift of Sardinia and the early history of the Western Mediterranean Basin. *Nature*, **298**, 736–9.

Clayton RN, O'Neil JR, Mayeda TK (1972) Oxygen isotope exchange between quartz and water. *Journal of Geophysical Research*, **77**, 3057–67.

Combes PJ (1969) *Recherches sur la genèse des bauxites dans le nord-est de l'Espagne, le Languedoc et l'Arìege (France)*. Dissertation. Université de Montpellier. 342 p.

Davatzes NC, Aydin A (2005) Distribution and nature of fault architecture in layered sandstone and shale sequence: an example from the Moab fault, Utah. In: *Faults, Fluid Flow, and Petroleum Traps* (eds Sorkhabi R, Tsuji Y) *AAPG Memoir*, **85**, 153–80.

Dewit J, Foubert A, El Desouky HA, Muchez Ph, Hunt D, Swennen R (2012) Dolomitisation model of hydrothermal dolomites (HTD) hosted by Aptian-Albian carbonates of the Ramales Platform (Basque-Cantabrian Basin, Northern Spain). VII Geofluids Conference, 75–8.

Dickson JAD (1966) Carbonate identification and genesis as revealed by staining. *Journal of Sedimentary Research*, **36**, 491–505.

Eichhubl P, Davatzes NC, Becker S (2009) Structural and diagenetic control of fluid migration and cementation along the Moab fault, Utah. *AAPG Bulletin*, **93**, 653–81.

Fernández M, Banda E (1989) An approach to the thermal field in northeastern Spain. *Tectonophysics*, **164**, 259–66.

Gaspar-Escribano JM, García-Castellanos D, Roca E, Cloetingh S (2004) Cenozoic vertical motions of the Catalan Coastal Ranges (NE Spain): the role of tectonics, isostasy, and surface transport. *Tectonics*, **23**, 1–18.

Jiménez de Cisneros C, Caballero E, Vera JA, Durán JJ, Juliá R (2003) A record of Pleistocene climate from a stalactite, Nerja Cave, southern Spain. *Palaeogeography, Palaeoclimatology, Palaeoecology*, **189**, 1–10.

Juez-Larré J (2003) *Post Late Paleozoic Tectonothermal Evolution of the Northeastern Margin of Iberia, Assessed by Fission-track and (U-Th)/He Analyses*. Dissertation, Vrije Universiteit, A case history from the Catalan Coastal Ranges. 200 p.

Julivert M, Durán H (1990) Paleozoic stratigraphy of the Central and Northern part of the Catalonian Coastal Ranges (NE Spain). *Acta Geologica Hispanica*, **25**, 3–12.

Labaume P, Moretti I (2001) Diagenesis-dependence of cataclastic thrust fault zone sealing in sandstones. Example from the Bolivian Sub-Andean Zone. *Journal of Structural Geology*, **23**, 1659–75.

Labaume P, Carrio-Schaffhauser E, Gamond JF, Renard F (2004) Deformation mechanisms and fluid-driven mass transfers in the recent fault zones of the Corinth Rift (Greece). *Comptes Rendus Geoscience*, **336**, 375–83.

Micarelli L, Benedicto A, Wibberley CAJ (2006) Structural evolution and permeability of normal fault zones in highly porous carbonate rocks. *Journal of Structural Geology*, **28**, 1214–27.

Mitjavila J, Martí J (1986) El volcanismo triásico del sur de Catalunya. *Revista d'Investigacions Geològiques*, **42–43**, 89–103.

Molina JM, Salas R (1993) Bauxitas kársticas del Cretácico inferior en Fuentespalda (provincia de Teruel): Estratigrafía, origen y paleogeografía. *Cuadernos de Geología Ibérica*, **17**, 207–30.

O'Kane A, Onasch CM, Farver JR (2007) The role of fluids in low temperature, fault-related deformation of quartz arenite. *Journal of Structural Geology*, **29**, 819–36.

Onasch CM, Dunne WM, Cook JE, O'Kane A (2009) The effect of fluid composition on the behaviour of well cemented, quartz-rich sandstone during faulting. *Journal of Structural Geology*, **31**, 960–71.

O'Neil JR, Clayton RN, Mayeda TK (1969) Oxygen isotope fractionation in divalent metal carbonates. *Journal of Chemical Physics*, **51**, 5547–58.

Ortí F, Vaquer R (1980) Volcanismo jurásico del sector valenciano de la Cordillera Ibérica. Distribución y trama estructural. *Acta Geológica Hispánica*, **XV**, 127–30.

Parcerisa D (2002) *Petrologia i diagènesi en sediments de l'Oligocè superior i del Miocè inferior i mitjà de la Depressió del Vallès i del Pla de Barcelona*. Dissertation, Universitat Autònoma de Barcelona, Evolució de l'àrea Font i dinámica dels fluids. 261 p.

Parry WT (1998) Fault-fluid compositions from fluid-inclusion observations and solubilities of fracture-sealing minerals. *Tectonophysics*, **290**, 1–26.

Piqué A, Canals A, Grandia F, Banks DA (2008) Mesozoic fluorite veins in NE Spain record regional base metal-rich brine circulation through basin and basement during extensional events. *Chemical Geology*, **257**, 139–52.

Ramon X, Calvet F (1987) Estratigrafía y sedimentología del Muschelkalk inferior del dominio Montseny-Llobregat (Catalánides). *Estudios geológicos*, **43**, 471–87.

Riba O, Colombo F (2009) *Barcelona: La Ciutat Vella i el Poblenou. Assaig de geologia urbana*, 1st edn. Institut d'Estudis Catalans. Reial Acadèmia de Ciències i Arts de Barcelona, Barcelona.

Roca E (1996) La evolución geodinámica de la Cuenca Catalano-Balear y áreas adyacentes desde el Mesozoico hasta la actualidad. *Acta Geológica Hispánica*, **29**, 3–25.

Roca E, Sans M, Cabrera L, Marzo M (1999) Oligocene to Middle Miocene evolution of the central Catalan margin (Northwestern Mediterranean). *Tectonophysics*, **315**, 209–33.

Rodríguez-Morillas N, Playà E, Travé A, Martín-Martín JD (2013) Diagenetic processes in a partially dolomitized carbonate reservoir: casablanca oil field, Mediterranean Sea, offshore Spain. *Acta Geologica*, **11**, doi: 10.1344/0.000001833.

Rossi C, Goldstein RH, Marfil R, Salas R, Benito MI, Permanyer A, de la Peña JA, Caja MA (2001) Diagenetic and oil migration history of the Kimmeridgian Ascla Formation, Maestrat Basin, Spain. *Marine and Petroleum Geology*, **18**, 287–306.

Rowland JV, Sibson RH (2004) Structural controls on hydrothermal flow in a segmented rift system, Taupo Volcanic Zone, New Zealand. *Geofluids*, **4**, 259–83.

Salas R, Casas A (1993) Mesozoic extensional tectonics, stratigraphy and crustal evolution during the Alpine cycle of the eastern Iberian basin. *Tectonophysics*, **228**, 33–55.

Salas R, Guimerà J, Mas R, Martín-Closas C, Meléndez A, Alonso A (2001) Evolution of the Mesozoic central Iberian Rift System and its Cainozoic inversion (Iberian Chain). In: *Peri-Tethys Memoir 6: Peri-Tethyan Rift/Wrench Basins and Passive Margins* (eds. Ziegler PA, Cavazza W, Robertson AHF, Crasquin-Soleau S) *Mémoires du Muséum National d'Histoire Naturelle*, **186**, 145–85.

Salas R, Vaquer R, Travé A (2004) Bauxitas kársticas y arcillas lateríticas barremienses de la Cadena Ibérica oriental y la Cadena Costero Catalana: relaciones genéticas y áreas de procedencia. *Geo-Temas*, **6**, 123–6.

Salas R, Caja MA, Martín JD, Mas R, Permanyer A (2005) Mid-Late Cretaceous volcanism, metamorphism and the regional thermal event affecting the Northeastern Iberian basins (Spain). In: *Global Events During the Quiet Aptian-Turonian Superchron* (eds Arnaud-Vanneau A, Arndt N, Zghal I). *Série spéciale colloques et excursions*, **6**, 55–8.

Santanach P, Casas JM, Gratacós O, Liesa M, Muñoz JA, Sàbat F (2011) Variscan and Alpine structure of the hills of Barcelona: geology in an urban area. *Journal of Iberian Geology*, **37**, 121–36.

Sibson RH (1986) Earthquakes and rock deformation in crustal fault zones. *Annual Review of Earth and Planetary Sciences*, **14**, 149–75.

Sibson RH, Moore JMcM, Rankin AH (1975) Seismic pumping-a hydrothermal fluid transport mechanism. *Journal of the Geological Society of London*, **131**, 653–9.

Solé J, Cosca M, Sharp Z, Enrique P (2002) 40Ar/39Ar geochronology and stable isotope geochemistry of Late-Hercynian intrusions from north-eastern Iberia with implications for argon loss in K-feldspar. *International Journal of Earth Sciences (Geol Rundsch)*, **91**, 865–81.

Swanson MT (1992) Fault structure, wear mechanisms and rupture processes in pseudotachylyte generation. *Tectonophysics*, **204**, 223–42.

Tavarnelli E, Pasqui V (2000) Fault growth by segment linkage in seismically active settings: examples from the Southern Apennines, Italy, and the Coast Ranges, California. *Journal of Geodynamics*, **29**, 501–16.

Taylor HP Jr (1977) Water/rock interactions and the origin of H_2O in granitic batholiths. *Journal of the Geological Society of London*, **133**, 509–58.

Travé A, Calvet F (2001) Syn-rift geofluids in fractures related to the early-middle Miocene evolution of the Vallès-Penedès half-graben (NE Spain). *Tectonophysics*, **336**, 101–20.

Travé A, Roca E, Playà E, Parcerisa D, Gómez-Gras D, Martín-Martín JD (2009) Migration of Mn-rich fluids through normal faults and fine-grained terrigenous sediments during early development of the Neogene Vallès-Penedès half-graben (NE Spain). *Geofluids*, **9**, 303–20.

Tucker M, Marshall J (2004) Diagenesis and geochemistry of Upper Muschelkalk (Triassic) buildups and associated facies in Catalonia (NE Spain): a paper dedicated to Francesc Calvet. *Geologica Acta*, **2**, 257–69.

Veizer J, Ala D, Azmy K, Bruckschen P, Buhl D, Bruhn F, Carden G, Diener A, Ebneth S, Godderis Y, Jasper T, Korte C, Pawellek F, Podlaha O, Strauss H (1999) $^{87}Sr/86Sr$, $\delta^{13}C$ and $\delta^{18}O$ evolution of Phanerozoic seawater. *Chemical Geology*, **161**, 59–88.

Vesica PL, Tuccimei P, Turi B, Fornós JJ, Ginés A, Ginés J (2000) Late Pleistocene Paleoclimates and sea-level change in the Mediterranean as inferred from stable isotope and U-series studies of overgrowths on speleothems, Mallorca, Spain. *Quaternary Science Reviews*, **19**, 865–79.

Virgili C (1957) *El Triásico de los Catalánides*. Dissertation, Universitat de Barcelona.

Zhang Y, Gartrell A, Underschultz JR, Dewhurst DN (2009) Numerical modelling of strain localisation and fluid flow during extensional fault reactivation: implications for hydrocarbon preservation. *Journal of Structural Geology*, **31**, 315–27.

GEOFLUIDS

Volume 14, Number 1, February 2014
ISSN 1468-8115

CONTENTS

WILEY Blackwell

Geofluids* is abstracted/indexed in *Chemical Abstracts

This journal is available online at Wiley Online Library. Visit onlinelibrary.wiley.com to search the articles and register for table of contents and e-mail alerts.